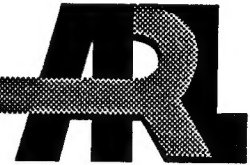




ARMY RESEARCH LABORATORY



**Monte Carlo Code for
Evaluating the Boundary Layer
Illumination and Radiation
Balance Model
(BLIRB)**

**by Michael B. Wells
Wells Consulting, Inc.**

ARL-CR-193

January 1995

19950501 018

DTIC QUALITY INSPECTED 8

Approved for public release; distribution is unlimited.

NOTICES

Disclaimers

The findings in this report are not to be construed as an official Department of the Army position, unless so designated by other authorized documents.

The citation of trade names and names of manufacturers in this report is not to be construed as official Government indorsement or approval of commercial products or services referenced herein.

Destruction Notice

When this document is no longer needed, destroy it by any method that will prevent disclosure of its contents or reconstruction of the document.

REPORT DOCUMENTATION PAGE			Form Approved OMB No. 0704-0188	
Public reporting burden for this collection of information is estimated to average 1 hour per response, including the time for reviewing instructions, searching existing data sources, gathering and maintaining the data needed, and completing and reviewing the collection of information. Send comments regarding this burden estimate or any other aspect of this collection of information, including suggestions for reducing this burden, to Washington Headquarters Services, Directorate for Information Operations and Reports, 1215 Jefferson Davis Highway, Suite 1204, Arlington, VA 22202-4302, and to the Office of Management and Budget, Paperwork Reduction Project (0704-0188), Washington, DC 20503.				
1. AGENCY USE ONLY (Leave blank)		2. REPORT DATE January 1995		3. REPORT TYPE AND DATES COVERED
4. TITLE AND SUBTITLE Monte Carlo Code for Evaluating the Boundary Layer Illumination and Radiation Balance Model (BLIRB)			5. FUNDING NUMBERS	
6. AUTHOR(S) Michael B. Wells				
7. PERFORMING ORGANIZATION NAME(S) AND ADDRESS(ES) Wells Consulting, Inc. 3812 Glenmont Drive Fort Worth, TX 76133			8. PERFORMING ORGANIZATION REPORT NUMBER Delivery Order 1223	
9. SPONSORING / MONITORING AGENCY NAME(S) AND ADDRESS(ES) U.S. Army Research Laboratory Battlefield Environment Directorate ATTN: AMSRL-BE WSMR, NM 88002-5501			10. SPONSORING / MONITORING AGENCY REPORT NUMBER ARL-CR-193	
11. SUPPLEMENTARY NOTES				
12a. DISTRIBUTION / AVAILABILITY STATEMENT Approved for public release; distribution is unlimited.			12b. DISTRIBUTION CODE A	
13. ABSTRACT (Maximum 200 words) The AGGIE Monte Carlo code was modified by providing an output file giving information on the location and direction of motion for each source photon and collided photon during a run. The CUBCLD1 code was developed to analyze the collision file to determine the polar and azimuthal angle distribution of the photons escaping from each side of a box-shaped cloud. The AGGIE code was modified to evaluate hemispheric emission from a box-shaped cloud. The modified code was used to provide calculational data for both a sunlight source and ground and cloud emission. The results were compared to data reported by McKee and Cox; Harshvardhan, Weinmann, and Davies; and Zardecki. The comparison shows that AGGIE is capable of providing accurate radiation transport data used for validating the BLIRB code.				
14. SUBJECT TERMS optical radiation, thermal radiation, monte carlo, clouds, aerosols, absorption, scattering, boundary layer, radiative transfer			15. NUMBER OF PAGES 99	
			16. PRICE CODE	
17. SECURITY CLASSIFICATION OF REPORT Unclassified	18. SECURITY CLASSIFICATION OF THIS PAGE Unclassified	19. SECURITY CLASSIFICATION OF ABSTRACT Unclassified	20. LIMITATION OF ABSTRACT SAR	

Acknowledgments

This work was supported by the Battlefield Environment Directorate (Dr. Patti Gillespie) under the auspices of the U.S. Army Research Office Scientific Services Program administrated by Battelle (Delivery Order 1223, Contract No. DAAL03-91-C-0034). The author is grateful to Patti Gillespie, David Tofsted, and Alan Wetmore for their illuminating discussions.

Accession For	
NTIS CRA&I	<input checked="checked" type="checkbox"/>
DTIC TAB	<input type="checkbox"/>
Unannounced	<input type="checkbox"/>
Justification	
By	
Distribution /	
Availability Codes	
Dist	Avail and/or Special
A-1	

Contents

Acknowledgments	1
1. Introduction	7
2. Calculational Methods	9
3. Calculations of Photon Leakage from Cubical Clouds	21
3.1 Validation of the Monte Carlo Calculations of Cloud Leakage ...	46
4. Calculations of Cloud and Ground Emission	61
4.1 Validation of the Monte Carlo Calculations of Hemispherical Power Emitted from the Top and Side of a Cubical Cloud	73
5. Conclusions and Recommendations	79
References	81
Acronyms and Abbreviations	83
Distribution	85

Figures

1. Cloud geometry for a cubical shaped cloud	23
2. Output file from CUBCLD1 for solar zenith angle of 0.0° , an optical thickness of 4.9 and side 1 of cloud	29
2a. Output file produced by SMCLOUD for zenith angle of 0.0° and cloud optical thickness of 4.9	30
3. Fraction of incident photons exiting cloud top, bottom, and sides: 0.0°	47
4. Fraction of incident photons exiting cloud top, bottom, and sides: 30°	48
5. Fraction of incident photons exiting cloud top, bottom, and sides: 60°	49

6.	Directional reflectance for zenith angle of 0.0°	50
7.	Directional reflectance for zenith angle of 30°	51
8.	Directional reflectance for zenith angle of 60°	52
9.	Photons exiting each side of cloud upward and downward: 0.0°	53
10.	Photons exiting each side of cloud upward: 30°	55
11.	Photons exiting each side of cloud downward: 30°	56
12.	Photons exiting each side of cloud upward: 60°	57
13.	Photons exiting each side of cloud downward: 60°	58
14.	Cumulative probability of photon scatter versus scattering angle	62
15.	Direct emitted power and emitted power versus order of scattering	65
16.	Effective blackbody temperature for upward hemispheric power at top of isolated cloud	73
17.	Effective blackbody temperature for upward hemispheric power at top of composite cloud	74
18.	Effective blackbody temperature for upward hemispheric power exiting side of isolated cloud	76
19.	Effective blackbody temperature for upward hemispheric power exiting side of composite cloud	77
20.	Effective blackbody temperature for the upward hemispheric power exiting the composite cloud side: Modified AGGIE data	78

Tables

1.	Comparison of Wells's and Davies's calculations of the cumulative probability of scattering for a wavelength of $0.45 \mu\text{m}$ in the C.1 water cloud	22
2.	Number of histories and collisions/history used in AGGIE problems	25
3.	Photon leakage and percent standard deviation for photons leaking out of sides of cloud: zenith angle = 0.0°	31
4.	Photon leakage and percent standard deviation for photons leaking out of sides of cloud: zenith angle = 30°	33
5.	Photon leakage and percent standard deviation for photons leaking out of sides of cloud: zenith angle = 60°	35
6.	Photon leakage and percent standard deviation for photons leaking out of sides of cloud: photons incident at a polar angle of 30° to the normal to side 1	38

7.	Photon leakage and percent standard deviation for photons leaking out of sides of cloud: photons incident at a polar angle of 60° to the normal to side 1	40
8.	Photon leakage from cloud for photons incident to both the top and side 1: solar zenith angle = 30°	42
9.	Photon leakage from cloud for photons incident to both the top and side 1: solar zenith angle = 60°	44
10.	Cloud hemispheric power from isolated cloud as seen by detectors on cloud top	63
11.	Cloud hemispheric power from composite cloud as seen by detectors on cloud top	68
12.	Comparison of hemispheric power at detectors on top of composite and isolated clouds	69
13.	Cloud hemispheric power from isolated cloud as seen by detectors on cloud side	70
14.	Cloud hemispheric power from composite cloud as seen by detectors on cloud side	71
15.	Comparison of hemispheric power at detectors on side of composite and isolated clouds	72

1. Introduction

The purpose of this report is to describe the modifications to A Generalized Geometry Irradiance Estimator (AGGIE) Monte Carlo codes. [1,2,3,4,5] These modifications were necessary so that AGGIE would be capable of providing radiation transport data used to evaluate the Boundary Layer Illumination Radiation Balance Model (BLIRB). [6,7] BLIRB is a part of the Low Observable Atmospheric Effects Model now used by the Battlefield Environment Directorate at White Sands Missile Range.

The tasks performed under Contract No. DAAL03-91-C0034, Delivery Order No. 1223, required that the Monte Carlo code be capable of calculating the angular distribution of the radiation leaving the six sides of box-shaped clouds positioned within the atmosphere as a function of position along each cloud face. The output data should be in harmony with BLIRB output. The computer model will include an atmosphere illuminated by a broad parallel beam of sunlight incident to the top of the atmosphere. It should also be capable of treating photon reflection by the surface of the earth that can reflect specularly, isotropically, or Lambertion. In the cloud region, the Monte Carlo code should treat photons that can scatter or be absorbed, and the interactions to be considered are absorption and scattering by molecules, scattering and absorption by atmospheric aerosols, and scattering and absorption by cloud particulates. The Monte Carlo code should be capable of evaluating the emitted thermal radiation by the atmosphere, clouds, and ground surface. In addition to being capable of computing the emitted radiation along a sensor line-of-sight, the code should be capable of evaluating the emitted radiation that is produced outside of the sensor line-of-sight and undergo one or more scattering events before scattering along the sensor line-of-sight into the sensor direction. The emitted radiation results shall be in harmony with BLIRB output.

The Monte Carlo code should be capable of determining the polar and azimuthal angle distribution of the radiation leakage from an area on a cloud side. The code should also be capable of treating problems involving the leakage from a box-shaped cloud when the cloud is illuminated by a broad

beam monochromatic source to the cloud top or to both the cloud top and a side of the cloud being illuminated.

Section 2 describes the AGGIE Monte Carlo code and the changes that were made so that it would be capable of treating the types of problems described. Section 3 describes calculations made using the modified AGGIE code that were run for comparison with data from McKee and Cox [8] and Davies [9] for the upward and downward photon leakage from the six sides of cubical-shaped clouds with optical thicknesses of 4.9, 10.0, 15.0, 25.0, 51.8, and 73.5. The clouds were illuminated by incident light at a wavelength of $0.45\text{ }\mu\text{m}$ for zenith angles of 0° , 30° , and 60° .

Section 4 describes the results of Monte Carlo calculations of the cloud and ground emitted radiation from a cubical-shaped cloud for a cloud optical thickness of 10.0 and an emission wavelength of $10.0\text{ }\mu\text{m}$. The cloud temperature was 250 K and the ground temperature was 300 K. The results of the emission calculations are compared with data from Harshvardhan et al. [10]

Section 5 gives some conclusions about the accuracy of the Monte Carlo calculations and some recommendations concerning the use of the Monte Carlo code to generate data for further validation of the BLIRB code.

2. Calculational Methods

AGGIE is a Monte Carlo program originally developed at Radiation Research Associates, Inc. to treat light transport problems having arbitrary, complex geometries. The original AGGIE code [1] was based on the TPART-3 code [11,12] that was developed to study time dependent light scattering in a plane-parallel atmosphere with a collimated source, a collimated receiver, and various reflecting targets. The geometrical flexibility of the entire series of AGGIE codes is derived from the melding of the TPART-3 with the combinatorial-geometry (CG) package of MORSE-CG. [13] MORSE-CG is an Oak Ridge National Laboratory program for the solution of neutron and gamma-ray transport problems. The resulting code permits arbitrary selection of various three-dimensional shapes from a set of nine basic body types and combines the enclosed or excluded volumes through unions and intersections to obtain a set of tailored geometrical zones. Each of these zones can be assigned distinct scattering, absorption, or boundary reflection characteristics. Terrain and atmospheric features, such as hills, buildings, vehicles, foliage, clouds, dust, and fog, can be modeled in considerable detail.

The original AGGIE program has been modified several times. One modification was the addition of a forward Monte Carlo mode. [3,4] Until then, the AGGIE code treated laser light scattering in the atmosphere problems with the backward mode where the n th or last collision point is selected by projecting a ray from the detector out through its field-of-view. Therefore, an estimate is made at the detector for each of the n collision points found. The backward mode is much more efficient than the forward mode when the detector field-of-view is small as in the case of a laser beam. The forward mode is very inefficient for limited field-of-view detectors. When the forward mode is used, the n th collision point is selected, as all previous collision points were selected, and an estimate is made of the contributions to the intensity at the detector only if the n th collision point is within the field-of-view of the detector.

One of the first steps in the evolution of the AGGIE program was an addition that enables the source angular distribution as an arbitrary non-Gaussian function to be specified. Previously, the source could only be treated as a

Gaussian distribution. Another modification made it possible to define zones wherein the concentration of scattering and/or absorbing particulates varies with geometrical position. [1] The design of this modification was such that other models for zones having spatially variable extinction characteristics can be easily interfaced with the program. These enhancements are documented in the technical report by Guinn and Collins.

Another major enhancement to the AGGIE code was the addition of an emission mode in which the path simulation process begins at the receiver and progresses outward. [2] The radiation source in this mode is from blackbody radiation emitted by the atmosphere, a cloud along each path segment, or the ground when it is intersected by a path segment. The estimates of the power incident on the detector are stored as a function of the zone from where they originated.

The AGGIE program treats multiple scattering of monochromatic light in a three-dimensional geometry of arbitrary complexity. Combinatorial geometry is used to construct zones or three-dimensional configurations through various unions, intersections, and differences of any of nine basic body shapes. The shapes include rectangular, parallel-piped, box, sphere, right circular cylinder, right elliptical cylinder, truncated right-angle cone, ellipsoid, right-angle wedge, and arbitrary polyhedron having four, five, or six sides. The geometrical zones are numbered, and each is identified with a medium distinguished by its optical characteristics.

Propagation of photons through the system requires the calculation of optical distances to zone boundaries as well as the identification of zones to be entered along the track. The photon is advanced from boundary to boundary until the interaction point determined by the selected path length is reached.

A medium number is associated with each geometrical zone, which identifies the set of optical characteristics assigned to that zone. A zone can be a scattering zone, a reflection zone, or a void. A photon will be reflected from the boundaries of a reflection zone, whereas, it will cross the boundaries of a scattering zone or void. A void is simply a scattering zone with its extinction, scattering, and absorption properties equal to zero.

A scattering zone is distinguished by its extinction, scattering, and absorption properties. AGGIE considers the effects caused by Rayleigh scattering, aerosol scattering, aerosol absorption, ozone absorption, and gaseous absorption. The parameters input for each zone are the extinction coefficient, which is the sum of all interaction coefficients; the ratio of the Rayleigh to total scattering coefficient, where the total scattering coefficient is the sum of the Rayleigh and aerosol scattering coefficients; the ratio of the total scattering coefficient to the extinction coefficient; and the aerosol phase matrix. Several phase-matrix tables can be read in allowing for a variety of scattering media (dust clouds, water clouds, haze, etc.) to be simulated.

A reflection zone and its surfaces can be designated with specular or diffuse reflection characteristics. Diffuse reflection can be isotropic, Lambertian, or arbitrary. Arbitrary reflection requires characterization by input data.

The albedo of a reflection surface can be defined according to the expression

$$ALBEDO = A_0 + A_1 \cos \theta_0 \quad (1)$$

where A_0 and A_1 are input constants keyed to a medium number associated with the zone, and θ_0 is the polar angle between the photons incident directions and the outward normal of the surface with which the photon is interacting. If A_1 is zero, the albedo is independent of the incident angle. The albedo is used in AGGIE to reduce the weight of the photon undergoing the reflection by multiplication.

AGGIE has also incorporated the TRACKS [14] and the HEDUST [15] models as a part of its geometrical capabilities. TRACKS represents the dust cloud generated by a moving tracked vehicle under certain parametrically specified conditions. HEDUST represents the cloud of smoke and dust generated by an impacting artillery sound. Details on the use of either of these models in AGGIE is referenced in *Utilization Instructions for the AGGIE-4 and ANACOL Computer Codes*. [5]

The AGGIE program uses a distinct source location to generate photons when operating in either the forward or backward modes. The source location can be a point, a source disk, or an area source positioned at any designated

altitude. The last of these source models was added during the current work. The detector can be a point detector or a finite area detector. In either case, the result is an intensity. A collision data output file, containing the following information for each source photon generated by the new area source (such as the top of a cloud), was added to AGGIE:

1. X coordinate of the source position
2. Y coordinate of the source position
3. Z coordinate of the source position
4. The batch number (NB)
5. The source particle number (NSP) in the batch
6. The collision number (NCOL)
7. The direction cosines (U, V, and W) of the photon direction
8. The photon weight (WAYT)
9. The number-of-histories-run counter (NPSCL(1))

After each collision, the above information is also written where the x,y,z coordinates are the coordinates of the collision point, and U, V, and W are the direction cosines for the photon's direction after collision.

The source emission is a Gaussian distribution along a diameter of the source disk (laser source), a point source with a user defined angular distribution, or an area source at a designated height. For a Gaussian distribution, the radial distance x to the point of emission on the source is sampled using the equation

$$X = \sqrt{-2\sigma^2 \ln(1 - RN(1 - \exp^{\frac{-D^2}{8\sigma^2}}))} \quad (2)$$

where

- | | | |
|----------|---|--|
| RN | = | a random number selected from a uniform distribution between 0 and 1 |
| σ | = | the standard deviation of the Gaussian distribution |
| D | = | the diameter of the source disk. |

The azimuthal position of the emission point is selected from a uniform distribution between 0.0 and 2π . The direction of the emitted photon is

assumed to be along the line through the point selected on the surface of the source disk and a pseudo source point located on the disk axis at a distance $S = (D/2)/\tan \theta_s$ behind the disk, where $D/2$ is the radius of the source disk and $\tan \theta_s$ is the divergence half-angle of the source cone.

All photons are emitted from the center of the source disk when the arbitrary source distribution is selected. The polar angle of emission is selected from a user supplied table of relative intensities. These intensities are in the form of a normalized cumulative probability distribution to facilitate the angle selection process. The distribution is assumed to be linear in each angle bin, and linear interpolation is used to select the exact angle within a given bin. The azimuthal angle is chosen from a uniform distribution between 0.0 and 2π . If the source emits radiation over a defined time interval, the emission time interval can be divided into NSET number of pulse heights (SIT(I)) at emission time SET(I). If the emission is not time dependent, the AGGIE results contain no source pulse dependence and may be folded with source data to obtain time-dependent results.

In the backward and emission modes, the detector configuration used by AGGIE for flux calculations is a flat disk with a conical field-of-view. The detector position, polar, and azimuthal directions of its normal, radius, and field-of-view half angle are required for their purpose. The detector area may also be partitioned into concentric rings and the flux reported for each ring.

The detector may be represented as both a point and/or a flat disk detector in the forward mode. The flat disk detector yields results in intensity (photon/unit area) and function just as the backward mode detector gives the results in the print out. If an estimate file is to be written, the point detector yields results in flux (photons). The flat disk detector restricts the receiver flux to that which enters the detector through a limited field-of-view, and the point detector accepts photons from any direction. Each forward estimate is recorded in an output estimate file. ANACOL, [5] an auxiliary program, is used to calculate the intensity or flux for a detector oriented in any direction and with any field-of-view. This option allows for certain parameters from each estimate to be saved for later studies of the photon distribution at the detector. The effects

of various detector aperture shapes and sizes can be investigated without having to repeat an entire AGGIE calculation.

The basic Monte Carlo random walk process used in AGGIE is described in *AGGIE-3 Technical Report on a Generalized Geometry Irradiance Estimator Monte Carlo Program*. [3] This process consists of creating a photon and following it along randomly generated paths as it scatters and reflects within the problem geometry. The tracking process begins with the selection of an emission direction from the source and a source position. A path length is determined from the appropriate distribution and the particle is moved to this location. A scattering event is simulated and the path simulation is repeated. If the photon intersects a reflection surface, the appropriate reflection event is simulated. For each interaction, an estimate is made of the radiation flux that the interaction would be expected to produce. For single scattering, the energy at the receiver is obtained by calculating the effective receiver area for each collision position. The method for making estimates of multiple scattering intensity depends on which mode the program is being operated in. However, in all these modes, the individual events that comprise the transport process are the same. The forward mode makes an estimate only if the current location is in the field-of-view of the detector. The position of the last collision is determined in the same manner as all previous points. In the backward mode, the location of the final or nth collision (in the case of multiple scattering) is obtained by starting a photon at a random point on the receiver disk and propagating it backwards along a direction randomly selected within the receiving field-of-view. The nth collision point, at the end of this backward path, is then connected with the n-1th collision point previously generated by forward propagation. The final receiver estimate depends in part on the geometrical characteristics of this connection and on the optical characteristics of the media in which it takes place.

If the program is to be run in the emission mode, the program is assumed to be run in the adjoint mode (the photons are emitted at the receiver and travel backwards to estimate the contribution of atmospheric and ground emission). Therefore, the meaning of the source and receiver input are reversed. The receiver disk area is normalized to 1 m² regardless of the size of the source

disk that may be input to AGGIE. When the emission option is selected (IEMIS > 0), no input for the receiver is needed.

For all calculations of emission, the source term is defined in units of W/m²-μm-sr. If the output is wanted in units of W/cm²-μm, STERN, an input parameter, should be input as 10⁻⁴. If the units are to be W/m²-μm, STERN should be input as 1.0.

In AGGIE, the radiant power at the detector resulting from emission at wavelength from each geometrical zone along the direction toward the detector is defined by the following equation:

$$s_0(\lambda) = \sum_{i=1}^I B(\lambda, T_i) \cos \theta_0 e^{-\sum_{j=0}^{i-1} l_j \sigma_{t,j}(\lambda)} (1 - e^{-l_i \sigma_{a,i}(\lambda)}) + B(\lambda, T_g) e^{-\sum_{j=0}^{I-1} l_j \sigma_{t,j}(\lambda)} \quad (3)$$

where

$B(\lambda, T)$	=	the Plank function for blackbody emission
T_i	=	the atmospheric temperature in zone i
T_g	=	the ground temperature
l_i	=	its distance along the direction to the detector through the ith zone
$\sigma_{t,i}(\lambda)$	=	the extinction coefficient for wavelength λ in the ith zone
$\sigma_{a,i}(\lambda)$	=	is the absorption coefficient for wavelength λ in the ith zone.

Note that $l_i = 0$ for $i = 0.0$. The units of S are W/m², and θ_0 is the polar angle of emission with respect to the normal to the zone boundary. When θ_0 is sampled from an isotropic distribution about the normal to the zone boundary,

$$B(\lambda, T_i) \cos \theta_0 \quad (4)$$

is the power in $W/m^2\text{-}\mu m$ at the i th zone surface. The function $B(\lambda, T)$ is the Plank blackbody function for radiation emitted through a unit surface area per steradian when the blackbody is at temperature T . $B(\lambda, T)$ is defined by the following equation:

$$B(\lambda, T) = \frac{1.190956 \times 10^{-12}}{\lambda^5 (e^{\frac{1.43879}{\lambda T}} - 1)} \quad (5)$$

in units of $W/m^2\text{-}\mu m\text{-sr}$, where λ is the wavelength in cm and T is in degrees Kelvin.

In subroutine SOURCG, a direction within the field-of-view of the emission detector is selected at random. The distribution

$$p(\theta_0) = 1 - \cos \theta_0 \quad (6)$$

is used to select random values of θ_0 , and the azimuth angle is selected uniformly between 0.0 and 2π .

A distance to collision from the detector location is selected at random from the distribution function for optical distances to collision. The type of scattering event occurring at the collision position is selected at random, and a random scattering angle, depending on the type of scattering event, is selected. An estimate of the emitted power reaching the detector from a first order scattering event is given by

$$EST_1 = \left(\frac{\sum_{S,1}}{\sum_{T,1}} \right) e^{-\rho_1} S_1 \quad (7)$$

where

$\Sigma_{S,1}$ = the scattering coefficient evaluated for the first collision location

$\Sigma_{T,1}$ = the extinction coefficient evaluated for the first collision location

- ρ_1 = the optical distance from the detector to the first collision position
- S_1 = the power per steradian reaching the collision position from emission sources along the direction selected from the first collision position.

S_1 is calculated with equation (7) for S_0 , except that the detector is assumed to be located at the first collision position.

After the estimate EST_1 is made, the random distance to the next collision and random polar and azimuthal scattering angles are selected. These values determine the location of the second collision. The type of scattering event that occurs at the second collision is selected at random. An estimate of the power that reaches the detector from the second collision is given by

$$EST_2 = \left(\frac{\sum_{S,1}}{\sum_{T,1}} \right) \left(\frac{\sum_{S,2}}{\sum_{T,2}} \right) e^{-(\rho_1 + \rho_2)} S_2 \quad (8)$$

where

- $\sum_{S,2}$ = the scattering coefficient at the location of the second collision event
- $\sum_{T,2}$ = the extinction coefficient at the location of the second collision event
- ρ_2 = the optical distance between the first and second collision positions.

This process is continued for $n_{\max}-1$ collisions. The estimate from the n th collision is given by

$$EST_n = \left(\frac{\sum_{S,1}}{\sum_{T,1}} \right) \left(\frac{\sum_{S,2}}{\sum_{T,2}} \right) \dots \left(\frac{\sum_{S,n}}{\sum_{T,n}} \right) x e^{-(\rho_1 + \rho_2 + \rho_3 + \dots + \rho_n)} S_n \quad (9)$$

The estimate of the emitted power per steradian reaching the detector from the direct emission and all n collisions for the K th history is given by

$$EST(K) = \sum_{n=1}^{NCMAX-1} EST_{K,n} + S_0 \quad (10)$$

The estimate of the average power in the detector field-of-view is given by

$$POWER = \frac{STERN * SSANG}{NPC * NBATCH} \sum_{k=1}^{NPC * NBATCH} EST(k) \quad (11)$$

Where SSANG is the solid angle for the detector field-of-view and STERN = 10^4 . NPC is the number of source photons per batch and NBATCH is the number of batches. Each estimate of the power at the detector contains contributions from each region along the path detected for each collision of each history. These contributions are stored in AGGIE as a function of the zone from which they originated and a collision number.

In AGGIE, the intensity and polarization characteristics of the scattered radiation are defined in terms of the polarization parameters I_{\perp} , I_{\parallel} , U, and V, which are related to the Stokes parameter I, Q, U, and V. AGGIE provides for the definition of a source that is initially polarized through input of the polarization parameters PEND1, PARA1, U1, and V1. The source can be assumed to emit unpolarized light by defining the polarization parameters (PEND1, PARA1, U1, V1) to be (0.5, 0.5, 0.0, 0.0), where $I_{\perp} = PEND1$, $I_{\parallel} = PARA1$, $U = V1 = 0.0$, $V = V1 = 0.0$, and $PEND1 + PARA1 = 1.0$.

Changes were made to the AGGIE input and the source subroutine (SOURCG.FOR) for problems involving a broad-beam area source positioned on the top of a cloud so that the parameters XS1, XS2, YS1, YS2, ZS, and θ could be input to define an area source at altitude ZS. The source then lies in a Z plane at height $Z = ZS$. The coordinates of a source point XS, YS, ZS are given by

$$\begin{aligned} XS &= (XS2 - XS1) * RN1 \\ YS &= (YS2 - YS1) * RN2 \\ ZS &= ZS \end{aligned}$$

where RN1 and RN2 are random numbers. The initial polar angle in the XZ plane through the source point XS, YS, ZS is denoted as θ . The direction cosines for each source photon are given by

$$U = \cos (90 - \theta)$$

$$V = 0.0$$

$$W = \cos (180 - \theta)$$

The polarization parameters PARA1, PEND1, U1, and V1, along with the source normalization parameter STERN, are defined in the AGGIE input data. At the beginning of each history, new values of XS, YS, and ZS are determined.

3. Calculations of Photon Leakage from Cubical Clouds

The principal objective of the modifications made to the AGGIE Monte Carlo code was the requirement that the code could be used to validate BLIRB. Before the modified AGGIE code could be used for evaluation of BLIRB, it was necessary to validate the AGGIE code by comparing AGGIE results for the leakage of photons from cubical clouds of various optical thicknesses with similar data reported by Davies, [9] McKee and Cox, [8] and Zardecki. [7]

The cloud leakage calculations were for a wavelength of $0.45 \mu\text{m}$. [7,8,9] The cloud model was the type C.1 cumulus cloud given by Deirmendjian. [16] Table T.35 in the book by Deirmendjian lists the values of the four phase matrix elements $P_1/4\pi$, $P_2/4\pi$, $P_3/4\pi$, and $P_4/4\pi$. These elements as a function of the scattering angle θ were written to a file, PHASEF.DAT, which was used as input to a FORTRAN code denoted as AG5INP.FOR. This code multiplied the phase matrix elements by 4π to obtain the parameters P_1 , P_2 , P_3 , and P_4 . The AG5INP code was used to integrate the sum of $(P_1(\theta)+P_2(\theta))/2.0$ over the polar scattering angle to obtain the cumulative distribution of the probability of photon scatter as a function of the 75 scattering angles used by Deirmendjian. The cosines of the angle for each of 50 intervals of equal probability were evaluated by AG5INP. The output file written by AG5INP is denoted as AG5INP.DAT. This file contains the portion of the problem input data deck for AGGIE that defines the optical properties of the cloud. Table 1 lists the cumulative probability of photon scatter as a function of the scattering angle for Deirmendjian type C.1 cloud as obtained from the data in the AG5INP.DAT file and as tabulated in table 2 of Davies's paper. [9] The agreement between the two calculations is reasonably good, and the data points out the fact that the C.1 cloud-phase function is highly forward because 67.9 percent of the scattering is in the first 20° and 85.9 percent occurs in the first 40° . It is interesting to note that Davies used a double Henyey-Greenstein phase function to represent the C.1 cloud phase function in his calculations, [9] and table 2 of his paper shows that the double Henyey-Greenstein phase function grossly underestimates the forward peak in the first 10° of the scattering angle.

Table 1. Comparison of Wells's and Davies's calculations of the cumulative probability of scattering for a wavelength of 0.45 μm in the C.1 water cloud

Scattering Angle ($^{\circ}$)	M. Wells P (theta)	Davies P (theta)
0.0	.00000	.000
5.0	.47999	.470
10.0	.53999	.530
15.0	.59999	
20.0	.67996	.654
30.0	.77998	
40.0	.85997	.851
50.0	.91989	
60.0	.93996	
70.0	.94799	
80.0	.95599	.955
90.0	.96178	
100.0	.96535	.968
120.0	.97250	
140.0	.97964	
160.0	.98974	.995
180.0	1.00000	1.000

In the AGGIE problems, it was assumed that the cubic cloud was 1.0 km in height and 1 km in width. The ratio of the scattering coefficient to the extinction coefficient was taken to be 1.0 because no absorption occurs in the C.1 cloud at a wavelength of 0.45 μm . AGGIE problems were run for cloud optical thicknesses of 4.9, 10.0, 15.0, 25.0, 51.8, and 73.5. These optical thicknesses corresponded to those utilized by McKee and Cox [8] and Davies. [9]

The Monte Carlo model of the cloud is shown in figure 1. The orientation of the cloud is such that the incident solar beam strikes at most the top and one side of the cloud. X_0 and Y_0 are the horizontal dimensions of the cloud, and Z_0 is the vertical dimension. For the problems run in this study, $X_0 = Y_0 = Z_0 = 1.0$. The area of the cloud top, AREA1, is 1.0. The area parallel to the cloud top that photons must pass through before entering the side

of the cloud, AREA2, is equal to $\tan \theta_0$. The total area the incident beam passes through is

$$TAREA = AREA1 + AREA2 = 1 + \tan \theta_0 \quad (12)$$

The fraction of the total number of photons incident to TAREA that passes through AREA1 and AREA2 is $1.0/(1.0 + \tan(\theta_0))$ and $(\tan(\theta_0)/(1 + \tan(\theta_0)))$, respectively.

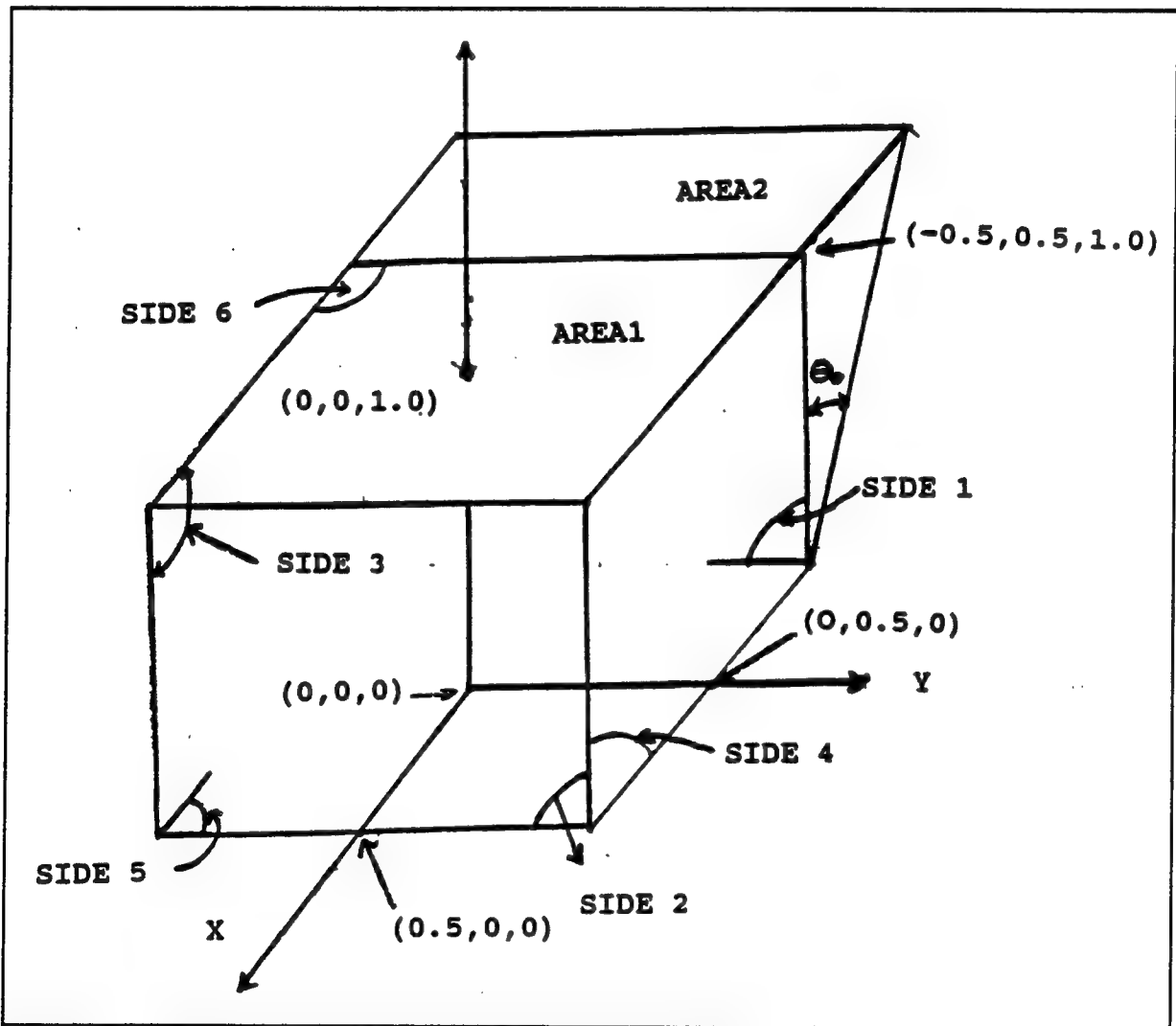


Figure 1. Cloud geometry for a cubical shaped cloud.

When θ_0 is greater than 0.0° , then its broad beam is incident to the cloud top (AREA1) at zenith angle and to the cloud side at a polar angle $= 90 - \theta_0$ with

respect to a normal to the cloud side. If $\theta_0 = 30^\circ$, $\theta_1 = 60^\circ$. Monte Carlo runs were made for $\theta_0 = 0.0^\circ$, 30.0° , and 60.0° . The cubical cloud for which the radiation is incident to the top of the cloud (side 6) was first rotated 90° clockwise about the $+x$ axis and rotated 90° counter-clockwise about the $+z$ axis so the source is incident to side 1 (at $x = -0.5$). The sides are then renumbered as follows:

S(I)	SS(I)
6	1
5	2
4	3
3	4
2	5
1	6

where S(I) is the side number originally assigned to the cloud and SS(I) is the side number after the two rotations of the cloud. The original source was on the cloud top (side 6). After the two rotations, original side 6 becomes side 1 in the YZ plane at $X = -0.5$, original side 5 becomes side 2 in the YZ plane at $x = +0.5$, original side 3 becomes side 4 in the XZ plane at $y = +0.5$, original side 4 becomes side 3 in the XZ plane at $y = -0.5$, original side 2 becomes side 5 in the XY plane at $Z = 0.0$, and the original side 1 becomes side 6 in the XY plane at $Z = 1.0$.

The total leakage out of side S(I), where $\theta_0 > 0^\circ$, is given by the following equation:

$$LN(I) = L(I) \left(\frac{1.0}{(1.0 + \tan \theta_0)} \right) + LT(I) \left(\frac{\tan \theta_0}{(1 + \tan \theta_0)} \right) \quad (13)$$

where L(I) is the leakage out of S(I) when the radiation is incident to the cloud top and LT(I) is the radiation leaking out of S(I) when the radiation is incident to the cloud side.

The total number of histories used in each of the Monte Carlo runs were divided into 10 batches.

Table 2 lists the maximum number of histories used for the optical thickness of each cloud. The number of collisions allowed per history and the maximum number of histories terminated by the photon weight falling below 1.0×10^{-5} are also listed. The number of histories terminated by the maximum number of collisions allowed parameter is given by the maximum number of histories ran minus the number terminated by the weights falling below the minimum weight value of 1.0×10^{-5} .

Table 2. Number of histories and collisions/history used in AGGIE problems

Cloud Optical Thickness	No. of Histories	No. of Cols. Per History	No. Hist. Term. by Min. Weight	Total No. Collisions
4.9	25,000	60	24999	219267
10.0	20,000	90	19999	262208
15.0	20,000	85	19987	344508
25.0	20,000	110	19868	507276
51.8	10,000	150	9437	442469
73.5	10,000	200	9263	576751

The collision data file output from AGGIE for each of the 18 problems run, which contained data describing the location of each source photon or scattered photon and the direction cosines of the photons direction of motion after being emitted from the source or after undergoing a scattering collision (see section 2), was read by a FORTRAN program, CUBCLD1. CUBCLD1 was developed to read the output file and to compute the probability of leaking out of the cloud side for each source position, collision position, and direction of motion after emission or scattering that would be intersected if the photon leaked from the cloud without undergoing another collision. CUBCLD1 determines which side of the cloud is intersected by the direction of the photon for each collision position as defined by the direction cosines. It assumes for the x and y planes forming sides 1, 2, 3, and 4 of the cubical cloud that the vertical line parallel to the z axis through the point of intersection of the direction of the photon with the plane measures the azimuthal angle in a clockwise direction. If the plane intersected is a z plane, sides 5 or 6, the line the azimuthal angle measures is parallel to the x axis. If each of the direction

cosines are positive, negative, or zero, CUBCLD1 determines the distances RX, RY, and RZ to the x, y, and z planes that could be intersected by the direction of the photons motion. The plane intersected is taken to be the plane for which the minimum of RX, RY, and RZ occurs.

The following equations are used to determine RX, RY, and RZ:

$$\begin{aligned}
 U > 0, RX &= (XMAX - X)/U \\
 U < 0, RX &= (X - XMIN)/-U \\
 U = 0, RX &= 1.0E + 06 \\
 V > 0, RY &= (YMAX - Y)/V \\
 V < 0, RY &= (Y - YMIN)/-V \\
 V = 0, RY &= 1.0E + 06 \\
 W > 0, RZ &= (ZMAX - Z)/W \\
 W < 0, RZ &= (Z - ZMIN)/-W \\
 W = 0, RZ &= 1.0E + 06.
 \end{aligned}$$

The distance DIST to the plane intersected along the photon path is the smallest of the values of RX, RY, and RZ. The optical distance to the cloud side intercepted by the photon direction of motion is $RHO = DIST * SIGT$. The photon weight FLUX exiting the cloud for the collision being considered is given by

$$FLUX = WAYT * e^{-RHO} \quad (14)$$

and the coordinates of the exit point are given by

$$\begin{aligned}
 XP &= (DIST * U) + X, \\
 YP &= (DIST * V) + Y, \text{ and} \\
 ZP &= (DIST * W) + Z.
 \end{aligned}$$

K is defined as follows depending on which side is intercepted:

$$\begin{aligned} K &= 1 \text{ if } (XP - XMIN) < 1.0E-05, \\ K &= 2 \text{ if } (XP - XMAX) < 1.0E-05, \\ K &= 3 \text{ if } (YP - YMIN) < 1.0E-05, \\ K &= 4 \text{ if } (YP - YMAX) < 1.0E-05, \\ K &= 5 \text{ if } (ZP - ZMIN) < 1.0E-05, \text{ and} \\ K &= 6 \text{ if } (ZP - ZMAX) < 1.0E-05. \end{aligned}$$

One must define three sets of direction cosines; these are determined by what side of the cloud the photon exits:

- UN, VN, and WN, the direction cosines of the outward pointing normal to the cloud side being exited.
- UA, VA, and WA, the direction cosines of the line connecting the points on the cloud side defined by the normal to the cloud side through the collision point and the point on the cloud side defined by the exit position of the photon exiting the cloud.
- The X, Y, and Z is the collision position on the cloud surface.
- UP, VP, and WP, the direction cosines of the line on the cloud side through the exit point from which the azimuthal angle AZIM of the exiting photon is to be measured.

The cosine of the polar angle between the outward normal to the cloud at the exit point and the photon's direction is given by

$$COSPOL = UN * U + VN * V + WN * W. \quad (15)$$

The cosine of the azimuthal angle AZIM is given by

$$COSAZIM = UA * UP + VA * VP + WA * WP. \quad (16)$$

The quadrant where AZIM lies depends on the values of x,y,z and XP,YP,ZP and the side being intersected. When

$K = 1, Y > Y_P, AZIM = 360 - AZIM,$
 $K = 2, Y < Y_P, AZIM = 360 - AZIM,$
 $K = 3, X < X_P, AZIM = 360 - AZIM,$
 $K = 4, X > X_P, AZIM = 360 - AZIM,$
 $K = 5, Y < Y_P, AZIM = 360 - AZIM, \text{ and}$
 $K = 6, Y_P > Y, AZIM = 360 - AZIM,$

otherwise the value of AZIM lies between 0.0° and 180.0° . CUBCLD determines the interval of the polar angle of exit PANG(I) and azimuthal angle AANG(J) where the calculated polar and azimuthal angles are to be stored.

Figure 2 shows the format of the output file from CUBCLD1 for a cloud optical thickness of 4.9 and a source zenith angle of 0.0° . The data shown in figure 2 are for side 1 of the cloud. Additional pages are generated for each side of the cloud. The data in figure 2 are listed in terms of the upper bounds of the azimuthal angle interval (twelve 30° -horizontal intervals) and the polar angle interval (nine 10° -vertical intervals). The fourth group of data in the figure lists the integral of the leakage over the azimuthal angle for each of the nine polar angle intervals listed. The total photon leakage for side 1 and the percent standard deviation of the total leakage from the side are given at the bottom of the figure. A similar table is output for each of the five other sides of the cloud. The sixth table also lists the total photon leakage from all six sides of the cloud. Each of the CUBCLD1 output files are input into SMCUBCLD, another FORTRAN code that computes the upward and downward photon leakage from each side of a cloud for a given cloud optical thickness and zenith angle of incidence. Figure 2a shows the SMCUBCLD output file for the case when the solar zenith angle is 0.0° and the cloud optical thickness is 4.9. The first line lists the upward leakage from sides 1, 2, 3, 4, and 6. The second line lists the downward leakage through sides 1, 2, 3, 4, and 5. The third and fourth lines in the figure list the total number of photons leaking upward and downward, respectively. The fifth through the tenth lines list the total flux leaking from the indicated side and the percent standard deviation of the total for that side. Side 5 is the bottom of the cloud, and figure 2a shows that 0.43745 photons/source photon are leaking out through the cloud bottom. The tenth line lists the total photon leakage, photon/source photon, from the cloud.

CLOUD OPTICAL THICKNESS = .49000E+01
 SOURCE POLAR ANGLE = .00000E+00 DEG.

PHOTON LEAKAGE FROM SIDE 1 AS A FUNCTION OF PANG AND AANG

	.30000E+02	.60000E+02	.90000E+02	.12000E+03
.10000E+02	.25785E-03	.12485E-03	.12676E-03	.25281E-03
.20000E+02	.46056E-03	.54107E-03	.45279E-03	.64965E-03
.30000E+02	.65735E-03	.63016E-03	.71896E-03	.90844E-03
.40000E+02	.63979E-03	.65112E-03	.82142E-03	.13373E-02
.50000E+02	.52707E-03	.56411E-03	.74984E-03	.11734E-02
.60000E+02	.65338E-03	.52845E-03	.53690E-03	.10633E-02
.70000E+02	.64959E-03	.33614E-03	.36122E-03	.73536E-03
.80000E+02	.30103E-03	.22885E-03	.18297E-03	.43509E-03
.90000E+02	.92888E-04	.82923E-04	.64812E-04	.12714E-03
SUM	.42395E-02	.36877E-02	.40157E-02	.66824E-02

	.15000E+03	.18000E+03	.21000E+03	.24000E+03
.10000E+02	.18207E-03	.19436E-03	.21213E-03	.20161E-03
.20000E+02	.68222E-03	.81794E-03	.73067E-03	.54715E-03
.30000E+02	.11825E-02	.15000E-02	.15867E-02	.12614E-02
.40000E+02	.16929E-02	.27000E-02	.28427E-02	.16930E-02
.50000E+02	.21382E-02	.43269E-02	.44262E-02	.25139E-02
.60000E+02	.23354E-02	.57796E-02	.52914E-02	.26005E-02
.70000E+02	.25094E-02	.66192E-02	.63439E-02	.25095E-02
.80000E+02	.17191E-02	.58419E-02	.57038E-02	.18987E-02
.90000E+02	.64017E-03	.29022E-02	.30145E-02	.69064E-03
SUM	.13082E-01	.30682E-01	.30152E-01	.13917E-01

	.27000E+03	.30000E+03	.33000E+03	.36000E+03
.10000E+02	.18201E-03	.17647E-03	.15227E-03	.17760E-03
.20000E+02	.65856E-03	.44696E-03	.48091E-03	.50823E-03
.30000E+02	.10468E-02	.84788E-03	.60440E-03	.60008E-03
.40000E+02	.10489E-02	.63707E-03	.61739E-03	.67896E-03
.50000E+02	.12423E-02	.66436E-03	.77801E-03	.56794E-03
.60000E+02	.11542E-02	.52439E-03	.53895E-03	.75376E-03
.70000E+02	.76765E-03	.34999E-03	.35914E-03	.66443E-03
.80000E+02	.37570E-03	.21987E-03	.20294E-03	.39821E-03
.90000E+02	.15460E-03	.52113E-04	.29359E-04	.10862E-03
SUM	.66307E-02	.39191E-02	.37634E-02	.44578E-02

.10000E+02	.22408E-02
.20000E+02	.69767E-02
.30000E+02	.11545E-01
.40000E+02	.15361E-01
.50000E+02	.19672E-01
.60000E+02	.21760E-01
.70000E+02	.22205E-01
.80000E+02	.17508E-01
.90000E+02	.79599E-02

TOTAL PHOTON LEAKAGE FOR SIDE 1 IS .12523E+00
 PERCENT STANDARD DEVIATION= .41837E+01
 CLOUD OPTICAL THICKNESS = .49000E+01

Figure 2. Output file from CUBCLD1 for solar zenith angle of 0.0°, an optical thickness of 4.9 and side 1 of cloud.

.24083E-01	.22798E-01	.23432E-01	.22821E-01	.69634E-01
.10115E+00	.10088E+00	.99346E-01	.98406E-01	.43745E+00
TOTAL PHOTONS SCATTERED UPWARD=				.16277E+00
TOTAL PHOTONS SCATTERED DOWNWARD=				.83723E+00
PHOTONS LEAKING FROM SIDE	1=	.12523E+00	.41837E+01	
PHOTONS LEAKING FROM SIDE	2=	.12368E+00	.49576E+01	
PHOTONS LEAKING FROM SIDE	3=	.12278E+00	.29749E+01	
PHOTONS LEAKING FROM SIDE	4=	.12123E+00	.31115E+01	
PHOTONS LEAKING FROM SIDE	5=	.43745E+00	.14492E+01	
PHOTONS LEAKING FROM SIDE	6=	.69634E-01	.71011E+01	
PHOTONS LEAKING FROM CLOUD=				.99999E+00

Figure 2a. Output file produced by SMCLOUD for zenith angle of 0.0° and cloud optical thickness of 4.9.

Tables 3, 4, and 5 list the photon leakage and percent standard deviation for each side of the cloud when = 0.0, 30.0 and 60.0 incident only to the top of the cloud. Also listed are the upward and downward leakages for each side and the total upward and downward leakage from all sides. Table 3 shows that the percent standard deviation exceeded a value of 10.0 when the solar zenith angle incident to the top of the cloud was 0.0° for side 5 when the optical thickness was 51.8 and for sides 3 and 5 when the optical distance was 73.5. Similarly, the percent standard deviation exceeded 10.0 in table 4 for side 1 when the optical thickness was 4.9, for side 5 when the optical thickness was 25, side 5 when the optical thickness was 51.8, and for side 5 when the optical thickness was 73.5. In table 5 the percent standard deviation exceeded 10 for side 1 when the optical thickness was 4.9, for sides 1 and 5 when the optical thickness was 10.0, for side 5 when the optical thickness was 15, for side 5 when the optical thickness was 25, for sides 1, 4, and 5 when the optical thickness was 51.8, and for sides 1, 3, and 5 when the optical thickness was 73.5. In general, the photon leakage from side 5, the cloud bottom, was the smallest in magnitude with respect to the magnitude of the leakage from the other sides.

Table 3. Photon leakage and percent standard deviation for photons leaking out of sides of cloud: zenith angle = 0.0°

Side No.	Total Photon Leakage	Percent Stand. Deviation	Leakage Upward	Leakage Downward
Optical Thickness = 4.9				
1	.12523+00	.41837+01	.24083-01	.10115+00
2	.12368+00	.49576+01	.22798-01	.10088+00
3	.12278+00	.29749+01	.23432-01	.99346-01
4	.12123+00	.31115+01	.22821-01	.98406-01
5	.43745+00	.14492+01		.43745+00
6	.69634-01	.71011+01	.69634-01	
Total	.99999+00		.16277+00	.83723+00
Optical Thickness = 10.0				
1	.16363+00	.34787+01	.41626-01	.12201+00
2	.16165+00	.34228+01	.39537-01	.12211+00
3	.16487+00	.25380+01	.41883-01	.12299+00
4	.16539+00	.19447+01	.40834-01	.12455+00
5	.22264+00	.19037+01		.22264+00
6	.12182+00	.34339+01	.12182+00	
Total	.10000+01		.28570+00	.71430+00
Optical Thickness = 15.0				
1	.17488+00	.28005+01	.50848-01	.12403+00
2	.17782+00	.37414+01	.53307-01	.12451+00
3	.17516+00	.40742+01	.50880-01	.12426+00
4	.17532+00	.41222+01	.51784-01	.13277+00
5	.12665+00	.46162+01		.12665+00
6	.16963+00	.65036+01	.16963+00	
Total	.99944+00		.37647+00	.62298+00
Optical Thickness = 25.0				
1	.17357+00	.23224+01	.59283-01	.11428+00
2	.17005+00	.39943+01	.57438-01	.11261+00
3	.17504+00	.21097+01	.59506-01	.11553+00
4	.16843+00	.33484+01	.56083-01	.11234+00
5	.60743-01	.52261+01		.60743-01
6	.24200+00	.20121+01	.24200+00	
Total	.98983+00		.47431+00	.51552+00

Table 3. Photon leakage and percent standard deviation for photons leaking out of sides of cloud: zenith angle = 0.0° (continued)

Side No.	Total Photon Leakage	Percent Stand. Deviation	Leakage Upward	Leakage Downward
Optical Thickness = 51.8				
1	.13332+00	.38576+01	.50561-01	.82763-01
2	.13489+00	.38486+01	.51445-01	.83449-01
3	.13377+00	.51868+01	.48476-01	.85292-01
4	.13694+00	.33913+01	.51612-01	.85333-01
5	.13705-01	.97657+01		.13705-01
6	.38509+00	.19072+01	.38509+00	
Total	.93773+00		.58718+00	.35054+00
Optical Thickness = 73.5				
1	.10862+00	.68876+01	.42251-01	.66369-01
2	.11237+00	.64359+01	.43308-01	.69067-01
3	.11244+00	.48703+01	.43340-01	.69097-01
4	.11060+00	.42041+01	.43166-01	.67437-01
5	.34407-02	.35243+02		.34407-02
6	.45727+00	.24980+01	.45729+00	
Total	.90476+00		.62935+00	.27541+00

Table 4. Photon leakage and percent standard deviation for photons leaking out of sides of cloud: zenith angle = 30°

Side No.	Total Photon Leakage	Percent Stand. Deviation	Leakage Upward	Leakage Downward
Optical Thickness = 4.9				
1	.34583-01	.66447+01	.13436-01	.21147-01
2	.47734+00	.10391+01	.31965-01	.44537+00
3	.10442+00	.35864+01	.20661-01	.83758-01
4	.10247+00	.50828+01	.19751-01	.82716-01
5	.21337+00	.17482+01		.21337+00
6	.67823-01	.48268+01	.67823-01	
Total	.10000+01		.15364+00	.84636+00
Optical Thickness = 10.0				
1	.65567-01	.41909+01	.24826-01	.40741-01
2	.39789+00	.12699+01	.53295-01	.34459+00
3	.14409+00	.40010+01	.37182-01	.10691+00
4	.14112+00	.44920+01	.35943-01	.10518+00
5	.12922+00	.34142+01		.12922+00
6	.12211+00	.46933+01	.12211+00	
Total	.99999+00		.27336+00	.72663+00
Optical Thickness = 15.0				
1	.82976-01	.75017+01	.32300-01	.50676-01
2	.34248+00	.29399+01	.60435-01	.28205+00
3	.15552+00	.56248+01	.46181-01	.10934+00
4	.15424+00	.33121+01	.45636-01	.10861+00
5	.86045-01	.57638+01		.86045-01
6	.17819+00	.42409+01	.17819+00	
Total	.99946+00		.36274+00	.63671+00
Optical Thickness = 25.0				
1	.94307-01	.38486+01	.36952-01	.57354-01
2	.28098+00	.33712+01	.66566-01	.21442+00
3	.15654+00	.35666+01	.51112-01	.10543+00
4	.15077+00	.46359+01	.50353-01	.10042+00
5	.47317-01	.52042+01		.47317-01
6	.26110+00	.37265+01	.26110+00	
Total	.99102+00		.46608+00	.52494+00

Table 4. Photon leakage and percent standard deviation for photons leaking out of sides of cloud: zenith angle = 30.0° (continued)

Side No.	Total Photon Leakage	Percent Stand. Deviation	Leakage Upward	Leakage Downward
<hr/> Optical Thickness = 51.8				
1	.85558-01	.23009+01	.36016-01	.49542-01
2	.19282+00	.43534+01	.54641-01	.13818+00
3	.12319+00	.44268+01	.46754-01	.76437-01
4	.12764+00	.37941+01	.46930-01	.80712-01
5	.96268-02	.17879+02		.96268-02
6	.40375+00	.15737+01	.40375+00	
Total	.94259+00		.58809+00	.35450+00
<hr/> Optical Thickness = 73.5				
1	.76021-01	.62200+01	.34061-01	.41961-01
2	.14683+00	.60356+01	.44970-01	.10186+00
3	.10215+00	.10003+02	.40070-01	.62084-01
4	.10726+00	.75543+01	.40734-01	.66525-01
5	.35226-02	.35444+02		.35226-02
6	.47331+00	.21260+01	.47331+00	
Total	.90909+00		.63315+00	.27595+00

Table 5. Photon leakage and percent standard deviation for photons leaking out of sides of cloud: zenith angle = 60°

Side No.	Total Photon Leakage	Percent Stand. Deviation	Leakage Upward	Leakage Downward
Optical Thickness = 4.9				
1	.19121-01	.11846+02	.65391-02	.12581-01
2	.71516+00	.64599+00	.56859-01	.65830+00
3	.72215-01	.39145+01	.14682-01	.57533-01
4	.70352-01	.44718+01	.14257-01	.56095-01
5	.34322-01	.90091+01		.34322-01
6	.88833-01	.44814+01	.88833-01	
Total	.10000+01		.18117+00	.81884+00
Optical Thickness = 10.0				
1	.33305-01	.59506+01	.12031-01	.21274-01
2	.55168+00	.13014+01	.75642-01	.47604+00
3	.10382+00	.61093+01	.27106-01	.76712-01
4	.10238+00	.39903+01	.27174-01	.75211-01
5	.39607-01	.74277+01		.39607-01
6	.16920+00	.28745+01	.16920+00	
Total	.10000+01		.31115+00	.68884+00
Optical Thickness = 15.0				
1	.45594-01	.63185+01	.16644-01	.28950-01
2	.45024+00	.15732+01	.78249-01	.37199+00
3	.11692+00	.32690+01	.34083-01	.82835-01
4	.11592+00	.56682+01	.33699-01	.82225-01
5	.36321-01	.11893+02		.36321-01
6	.23494+00	.30841+01	.23494+00	
Total	.99993+00		.39762+00	.60232+00
Optical Thickness = 25.0				
1	.52132-01	.62960+01	.21603-01	.30528-01
2	.33809+00	.27284+01	.73248-01	.26484+00
3	.12181+00	.46327+01	.41156-01	.80658-01
4	.11988+00	.24738+01	.40395-01	.79483-01
5	.25917-01	.13287+02		.25917-01
6	.33649+00	.21963+01	.33649+00	
Total	.99432+00		.51289+00	.48142+00

Table 5. Photon leakage and percent standard deviation for photons leaking out of sides of cloud: zenith angle = 60° (continued)

Side No.	Total Photon Leakage	Percent Stand. Deviation	Leakage Upward	Leakage Downward
Optical Thickness = 51.8				
1	.55040-01	.71789+01	.22154-01	.32887-01
2	.20842+00	.41849+01	.55573-01	.15284+00
3	.98844-01	.55845+01	.36824-01	.62019-01
4	.10132+00	.54801+01	.38605-01	.62718-01
5	.66950-02	.21596+02		.66950-02
6	.48680+00	.29622+01	.48680+00	
Total	.95712+00		.63996+00	.31716+00
Optical Thickness = 73.5				
1	.47131-01	.11619+02	.20813-01	.26318-01
2	.16759+00	.55825+01	.47793-01	.11980+00
3	.82617-01	.43984+01	.30748-01	.51869-01
4	.82546-01	.63109+01	.33147-01	.49399-01
5	.17854-02	.39603+02		.17854-02
6	.55479+00	.24030+01	.55479+00	
Total	.93646+00		.68729+00	.24917+00

A FORTRAN code, SUMCUB1, was written to rotate the data for zenith angles of $\theta_0 = 30^\circ$ and 60° to the top of the cloud to give data for polar angles of 30° and 60° incident to side 1 of the cloud. The results are shown in tables 6 and 7 for the photon exiting the cloud upward and downward from each side, the total photon leakage for each side, and the percent standard deviation of the total side leakage when the optical thicknesses were 4.9, 10, 15, 25, 51.8, and 73.5.

The data in table 6 for solar zenith angles of 30° incident to the cloud top and the data in table 7 for $90 - \theta_0 = 60^\circ$ incident to side 1 were combined by multiplying the data from table 6 for $\theta_0 = 30^\circ$ by the factor $(1.0/(1.0 + \tan(\theta_0)))$ and multiplying the data from table 7 for $90 - \theta_0 = 60^\circ$ by the factor $(\tan(\theta_0)/(1 + \tan(\theta_0)))$ and then adding the resulting data for each side and optical distance together. Similarly, the data in table 5 for $\theta_0 = 60^\circ$ to the cloud top were multiplied by the factor $(1.0/(1.0 + \tan(\theta_0)))$, the data from table 6 for $90 - \theta_0 = 30^\circ$ were multiplied by the factor $(\tan(\theta_0)/(1 + \tan(\theta_0)))$, and the resulting data for each side and optical thickness were added together. Tables 8 and 9 show the leakage results for $\theta_0 = 30^\circ$ and 60° when the source radiation is incident to both the top and sides of the clouds, respectively.

An examination of the data in table 3 shows that the leakage out of sides 1, 2, 3, and 4 when $\theta_0 = 0.0^\circ$ is approximately equal for each cloud optical thickness, as expected. Tables 4 and 5 for $\theta_0 = 30^\circ$ and 60° , respectively, show that the leakage out of sides 3 and 4 are approximately equal. In tables 6 and 7 for $\theta_1 = 90 - \theta_0 = 30^\circ$ and 60° with respect to the normal to side 1, it was also found that the leakage out of sides 3 and 4 were approximately equal. The photons incident to both the top and side 1 of the cloud when the solar zenith angle is 30° and 60° in tables 8 and 9, respectively, show the leakage out of sides 3 and 4 was approximately equal.

Table 6. Photon leakage and percent standard deviation for photons leaking out of sides of cloud: photons incident at a polar angle of 30° to the normal to side 1

Side No.	Total Photon Leakage	Percent Stand. Deviation	Leakage Upward	Leakage Downward
Optical Thickness = 4.9				
1	.67823-01	.48268+01	.41434-01	.26390-01
2	.21337+00	.17482+01	.15188+00	.61485-01
3	.10247+00	.50828+01	.33438-01	.69029-01
4	.10442+00	.35864+01	.33993-01	.70426-01
5	.47734+00	.10391+01		.47734+00
6	.34583-01	.66447+01	.34583-01	
Total	.10000+01		.29533+00	.70467+00
Optical Thickness = 10.0				
1	.12211+00	.46933+01	.70624-01	.51483-01
2	.12922+00	.34142+01	.72531-01	.56687-01
3	.14112+00	.44920+01	.54409-01	.86715-01
4	.14409+00	.40010+01	.55488-01	.88599-01
5	.39789+00	.12699+01		.39789+00
6	.65567-01	.41909+01	.65567-01	
Total	.99999+00		.31862+00	.68137+00
Optical Thickness = 15.0				
1	.17819+00	.42409+01	.96766-01	.81430-01
2	.86045-01	.57638+01	.44412-01	.41634-01
3	.15424+00	.33121+01	.61207-01	.93036-01
4	.15552+00	.56248+01	.61196-01	.94326-01
5	.34248+00	.29399+01		.34248+00
6	.82976-01	.75017+01	.82976-01	
Total	.99946+00		.34656+00	.65291+00
Optical Thickness = 25.0				
1	.26110+00	.37265+01	.13727+00	.12383+00
2	.47317-01	.52042+01	.23820-01	.23497-01
3	.15077+00	.46359+01	.64701-01	.86073-01
4	.15654+00	.35666+01	.66689-01	.89849-01
5	.28098+00	.33712+01		.28098+00
6	.94307-01	.38486+01	.94307-01	
Total	.99102+00		.38679+00	.60423+00

Table 6. Photon leakage and percent standard deviation for photons leaking out of sides of cloud: photons incident at a polar angle of 30° to the normal to side 1 (continued)

Side No.	Total Photon Leakage	Percent Stand. Deviation	Leakage Upward	Leakage Downward
Optical Thickness = 51.8				
1	.40375+00	.15737+01	.20728+00	.19647+00
2	.96268-02	.17879+02	.44407-02	.51862-02
3	.12764+00	.37941+01	.57648-01	.69958-01
4	.12319+00	.44268+01	.55642-01	.67549-01
5	.19282+00	.43535+01		.19282+00
6	.85558-01	.23009+01	.85558-01	
Total	.94259+00		.41057+00	.53202+00
Optical Thickness = 73.5				
1	.47331+00	.21260+01	.24140+00	.23191+00
2	.35226-02	.35444+02	.16730-02	.18496-02
3	.10726+00	.75543+01	.57425-01	.49835-01
4	.10215+00	.10003+02	.46229-01	.55925-01
5	.14683+00	.60356+01		.14683+00
6	.76021-01	.62200+01	.76021-01	
Total	.90910+00		.42275+00	.48635+00

Table 7. Photon leakage and percent standard deviation for photons leaking out of sides of cloud: photons incident at a polar angle of 60° to the normal to side 1

Side No.	Total Photon Leakage	Percent Stand. Deviation	Leakage Upward	Leakage Downward
Optical Thickness = 4.9				
1	.88833-01	.44814+01	.42551-01	.46281-01
2	.34322-01	.90091+01	.20393-01	.13930-01
3	.70352-01	.44718+01	.17975-01	.52377-01
4	.72215-01	.39145+01	.18985-01	.53230-01
5	.71516+00	.64599+01		.71516+00
6	.19121-01	.11846+02	.19121-01	
Total	.10000+01		.11902+00	.88098+00
Optical Thickness = 10.0				
1	.16920+00	.28745+01	.76249-01	.92953-01
2	.39607-01	.74277+01	.19582-01	.20026-01
3	.10238+00	.39903+01	.33405-01	.68980-01
4	.10382+00	.61093+01	.32510-01	.71308-01
5	.55168+00	.13014+01		.55168+00
6	.33305-01	.59506+01	.33305-01	
Total	.10000+01		.19505+00	.80495+00
Optical Thickness = 15.0				
1	.23494+00	.30841+01	.10494+00	.13001+00
2	.36321-01	.11893+02	.17021-01	.19300-01
3	.11592+00	.56682+01	.40233-01	.75692-01
4	.11692+00	.32690+01	.41669-01	.75250-01
5	.45024+00	.15732+01		.45024+00
6	.45594-01	.63185+01	.45594-01	
Total	.99994+00		.24945+00	.75049+00
Optical Thickness = 25.0				
1	.33649+00	.21963+01	.14759+00	.18890+00
2	.25917-01	.13287+02	.12915-01	.13001-01
3	.11988+00	.24738+01	.46550-01	.73329-01
4	.12181+00	.46327+01	.46540-01	.75273-01
5	.33809+00	.27284+01		.33809+00
6	.52132-01	.62960+01	.52132-01	
Total	.99432+00		.30573+00	.68859+00

Table 7. Photon leakage and percent standard deviation for photons leaking out of sides of cloud: photons incident at a polar angle of 60° to the normal to side 1 (continued)

Side No.	Total Photon Leakage	Percent Stand. Deviation	Leakage Upward	Leakage Downward
Optical Thickness = 51.8				
1	.48680+00	.29622+01	.21788+00	.26893+00
2	.66950-02	.21596+02	.31603-02	.35346-02
3	.10132+00	.54801+01	.43342-01	.57980-01
4	.98844-01	.55845+01	.41201-01	.57642-01
5	.20842+00	.41849+01		.20842+00
6	.55040-01	.71789+01	.55040-01	
Total	.95712+00		.36062+00	.59651+00
Optical Thickness = 73.5				
1	.55479+00	.24030+01	.24472+00	.31007+00
2	.17854-02	.39603+02	.73895-03	.10464-02
3	.82546-01	.63109+01	.36035-01	.46512-01
4	.82617-01	.43984+01	.35523-01	.47094-01
5	.16759+00	.55825+01		.16759+00
6	.47131-01	.11619+02	.47131-01	
Total	.93646+00		.36415+00	.57232+00

Table 8. Photon leakage from cloud for photons incident to both the top and side 1: solar zenith angle = 30°

Side No.	Leakage Upward	Leakage Downward	Leakage From Sides
Optical Thickness = 4.9			
1	.24093-01	.30347-01	.54400-01
2	.27729-01	.28745+00	.31518+00
3	.19678-01	.72272-01	.91950-01
4	.19471-01	.71923-01	.91396-01
5		.39704+00	.39704+00
6	.49997-01		.49997-01
Total	.14097+00	.85903+00	.10000+01
Optical Thickness = 10.0			
1	.43648-01	.59852-01	.10350+00
2	.40955-01	.22579+00	.26675+00
3	.35800-01	.93027-01	.12882+00
4	.34686-01	.92782-01	.12747+00
5		.28385+00	.28358+00
6	.89605-01		.89605-01
Total	.24470+00	.75530+00	.99999+00
Optical Thickness = 15.0			
1	.58888-01	.79714-01	.13860+00
2	.44544-01	.18588+00	.23042+00
3	.44004-01	.97024-01	.14103+00
4	.44184-01	.96399-01	.14058+00
5		.21935+00	.21935+00
6	.12966+00		.12966+00
Total	.32127+00	.67836+00	.99964+00
Optical Thickness = 25.0			
1	.77448-01	.10550+00	.18295+00
2	.46928-01	.14070+00	.18762+00
3	.49442-01	.93680-01	.14312+00
4	.48957-01	.91216-01	.14017+00
5		.15375+00	.15375+00
6	.18461+00		.18461+00
Total	.40739+00	.58484+00	.99223+00

Table 8. Photon leakage from cloud for photons incident to both the top and side 1: solar zenith angle = 30° (continued)

Side No.	Leakage Upward	Leakage Downward	Leakage From Sides
<hr/> Optical Thickness = 51.8			
1	.10258+00	.12984+00	.23242+00
2	.35798-01	.88896-01	.12469+00
3	.45505-01	.69681-01	.11519+00
4	.44833-01	.72268-01	.11710+00
5		.82390-01	.82390-01
6	.27611+00		.27611+00
Total	.50483+00	.44308+00	.94791+00
<hr/> Optical Thickness = 73.5			
1	.11117+00	.14010+00	.25126+00
2	.28780-01	.64960-01	.93740-01
3	.38593-01	.56384-01	.94974-01
4	.38827-01	.59413-01	.98240-01
5		.63575-01	.63575-01
6	.31732+00		.31732+00
Total	.53469+00	.38443+00	.91911+00

Table 9. Photon leakage from cloud from photons incident to both the top and side 1: solar zenith angle = 60°

Side No.	Leakage Upward	Leakage Downward	Leakage From Sides
Optical Thickness = 4.9			
1	.28662-01	.21336-01	.49997-01
2	.11710+00	.27993+00	.39704+00
3	.26573-01	.64821-01	.91396-01
4	.26769-01	.65180-01	.91950-01
5		.31518+00	.31518+00
6	.54440-01		.54440-01
Total	.25354+00	.74646+00	.10000+01
Optical Thickness = 10.0			
1	.49177-01	.40426-01	.89605-01
2	.73670-01	.21018+00	.28385+00
3	.44415-01	.83054-01	.12747+00
4	.45124-01	.83699-01	.12882+00
5		.26675+00	.26675+00
6	.10350+00		.10350+00
Total	.31589+00	.68410+00	.99999+00
Optical Thickness = 15.0			
1	.73170-01	.70173-01	.14334+00
2	.50277-01	.12963+00	.17991+00
3	.75886-01	.78825-01	.15471+00
4	.76504-01	.78551-01	.15505+00
5		.24862+00	.24862+00
6	.11783+00		.11783+00
Total	.39367+00	.60580+00	.99947+00
Optical Thickness = 25.0			
1	.94933-01	.89679-01	.18461+00
2	.41912-01	.11183+00	.15375+00
3	.56083-01	.84091-01	.14017+00
4	.57065-01	.86055-01	.14312+00
5		.18762+00	.18762+00
6	.18295+00		.18295+00
Total	.43295+00	.55928+00	.99223+00

Table 9. Photon leakage from cloud from photons incident to both the top and side 1: solar zenith angle = 60° (continued)

Side No.	Leakage Upward	Leakage Downward	Leakage From Sides
<hr/> Optical Thickness = 51.8			
1	.13952+00	.13659+00	.27611+00
2	.23156-01	.59231-01	.82390-01
3	.50026-01	.67076-01	.11710+00
4	.49406-01	.65781-01	.11519+00
5		.12469+00	.12469+00
6	.23242+00		.23242+00
Total	.49453+00	.45338+00	.94791+00
<hr/> Optical Thickness = 73.5			
1	.16066+00	.15666+00	.31732+00
2	.18554-01	.45022-01	.63575-01
3	.42849-01	.55391-01	.98240-01
4	.41441-01	.53536-01	.94974-01
5		.93740-01	.93740+00
6	.25126+00		.25126+00
Total	.51477+00	.40435+00	.91912+00

3.1 Validation of the Monte Carlo Calculations of Cloud Leakage

McKee and Cox [8] report the results of a series of Monte Carlo calculations of the leakage of photons through the six sides of a cubical cloud resulting from photons being incident to the top and side 1 of the cloud for zenith angles of 0.0° , 30° , and 60° . Figure 3 shows a comparison of the AGGIE results for the photons leaking out of the sides, top, and bottom of the cubical cloud as a function of the cloud optical thickness with similar data from the McKee and Cox calculations for a solar zenith angle of 0.0° . Also shown are BLIRB results for a solar zenith angle of 0.0° as reported by Zardecki. [7] In general, the AGGIE calculations versus the cloud optical thickness shown in figure 3 are in better agreement with the McKee and Cox data than with the BLIRB results. One possible reason is the fact that BLIRB is an eight-stream calculation of the scattered radiation and the two Monte Carlo calculations sample photon directions out of a continuous distribution of scattering angles.

Similar comparisons of calculations of the photons exiting the top, bottom, and four sides of the cubical cloud for solar zenith angles of 30° and 60° are shown in figures 4 and 5, respectively. The BLIRB calculations of the photons exiting the top for a solar zenith angle of 30° are always larger than those given by the AGGIE calculations and the McKee and Cox data.

Figures 6, 7, and 8 compare the AGGIE data and McKee and Cox data for the directional reflectance from the cloud (upward leakage from sides 1, 2, 3, and 4 and the top (side 6) of the cloud) as a function of the cloud optical thickness. In general, the McKee and Cox data are slightly higher than the AGGIE data.

Figure 9 shows a comparison of the AGGIE calculation of the leakage out of each side of the cloud versus optical thickness when the solar zenith angle is 0.0° . Data for both the upward and downward exiting photons are shown. The AGGIE data for the upward leaking photons is always less than that given by the McKee and Cox data. The downward leaking photons as given by AGGIE are greater than the McKee and Cox data for optical thicknesses to 51.8.

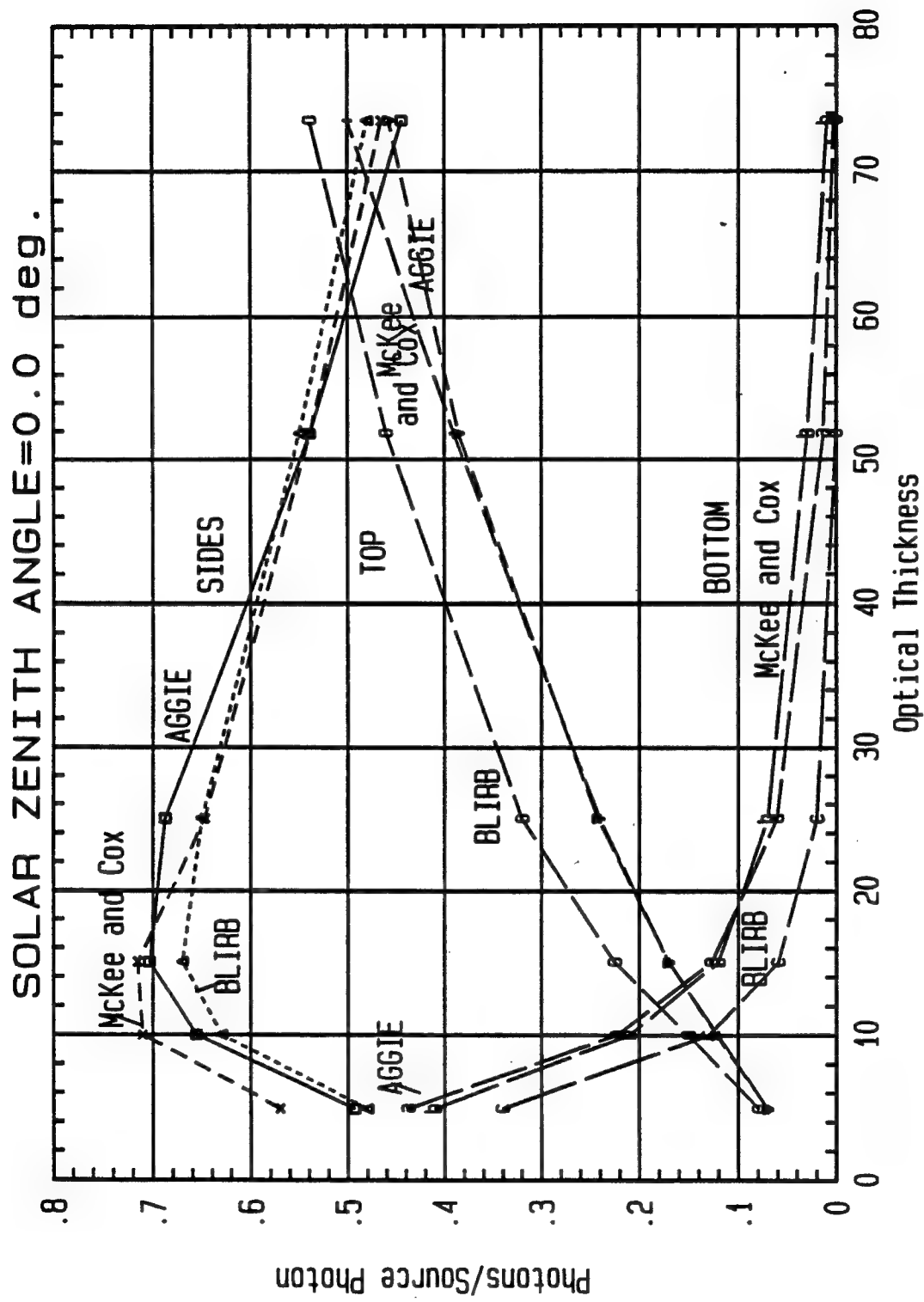


Figure 3. Fraction of incident photons exiting cloud top, bottom, and sides: 0.0°.

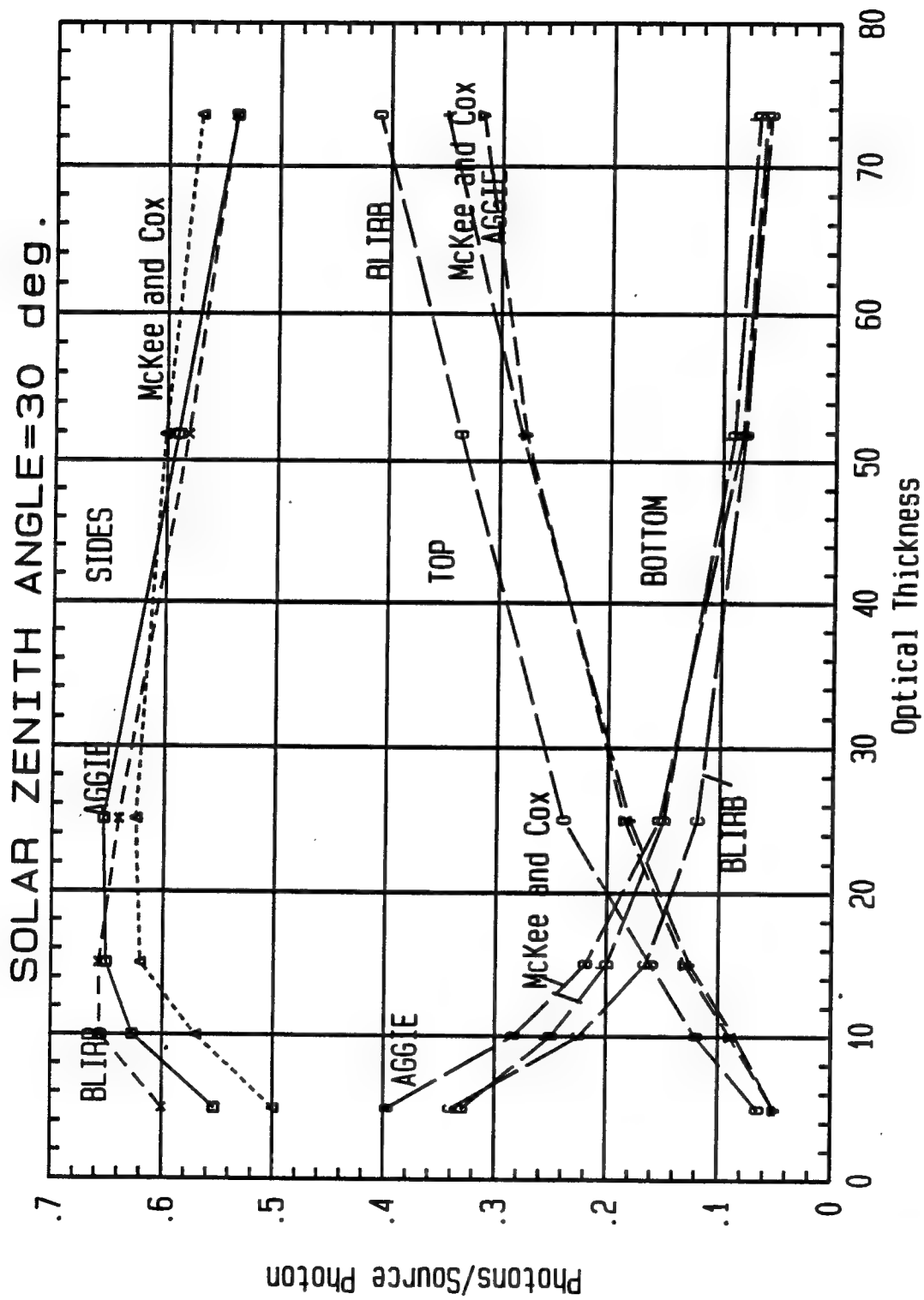


Figure 4. Fraction of incident photons exiting cloud top, bottom, and sides: 30°.

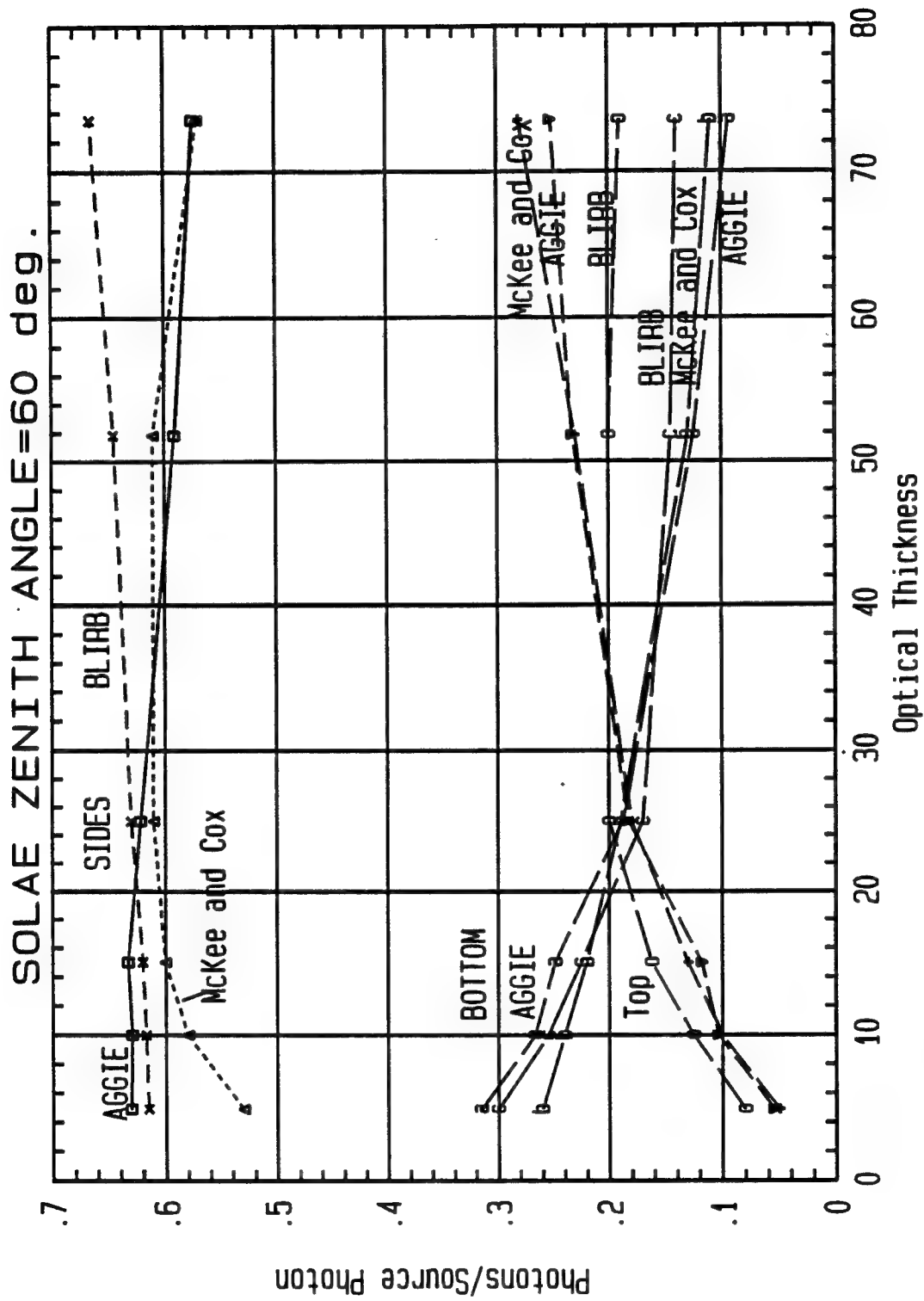


Figure 5. Fraction of incident photons exiting cloud top, bottom, and sides: 60°.

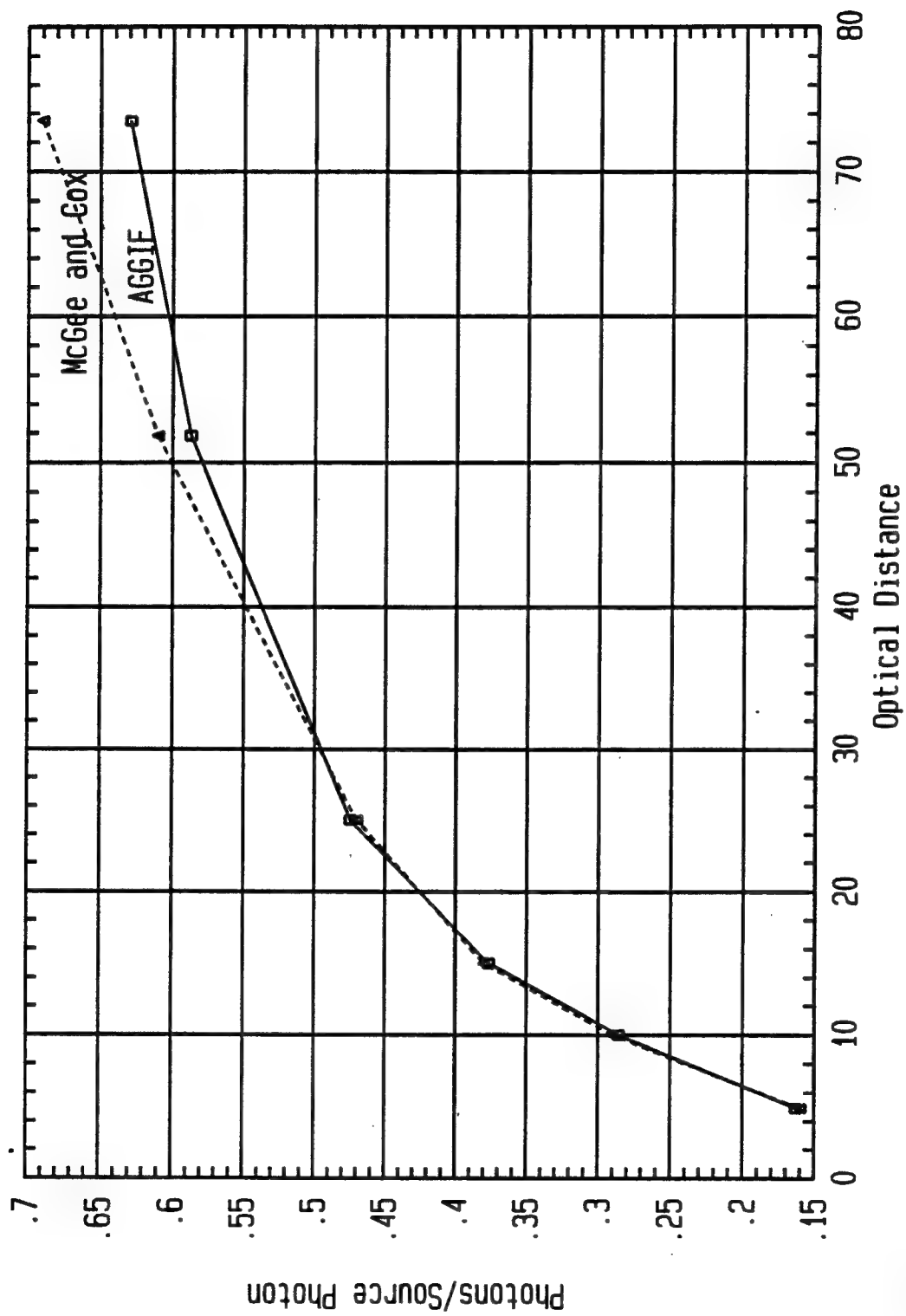


Figure 6. Directional reflectance for zenith angle of 0.0°.

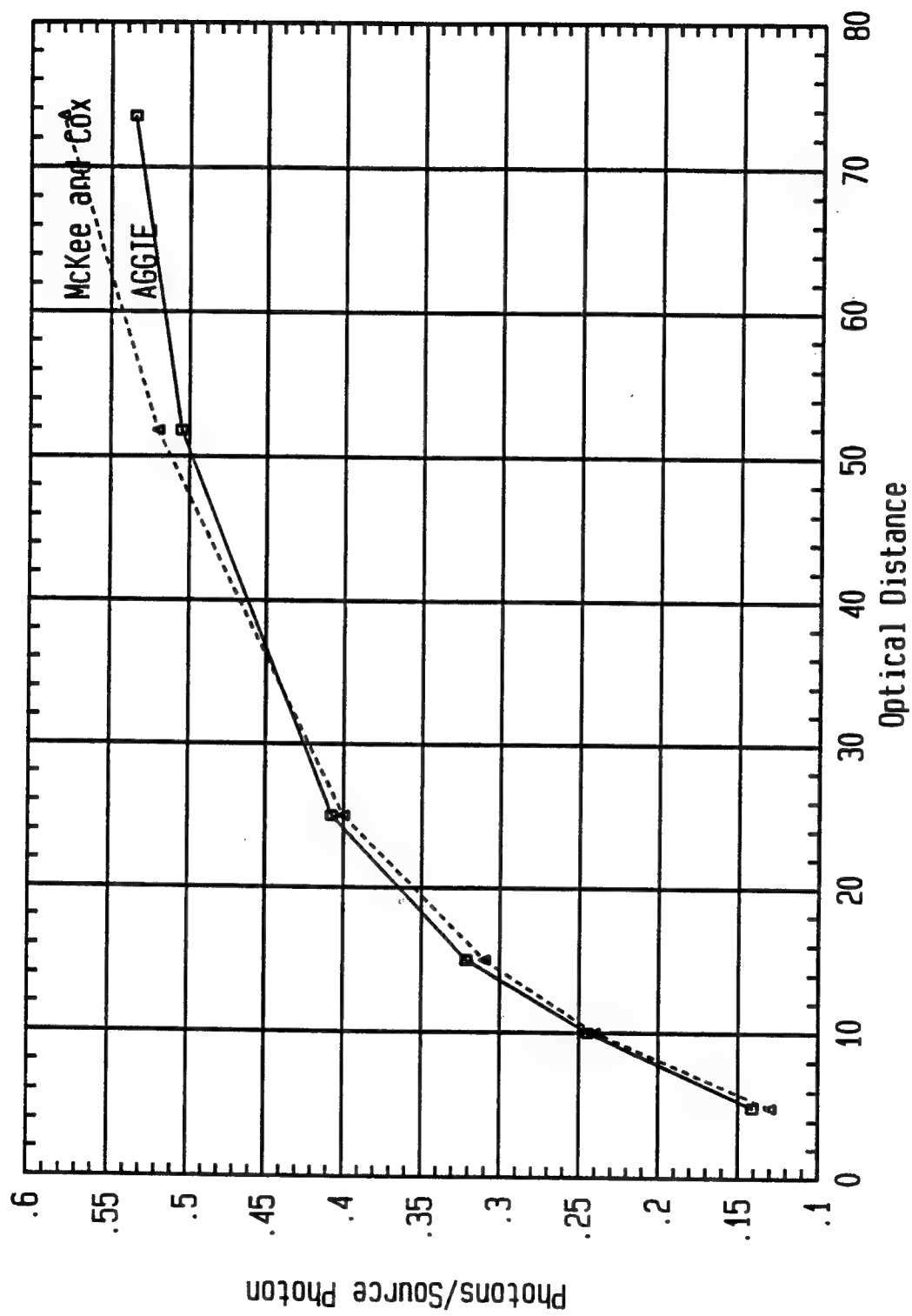


Figure 7. Directional reflectance for zenith angle of 30°.

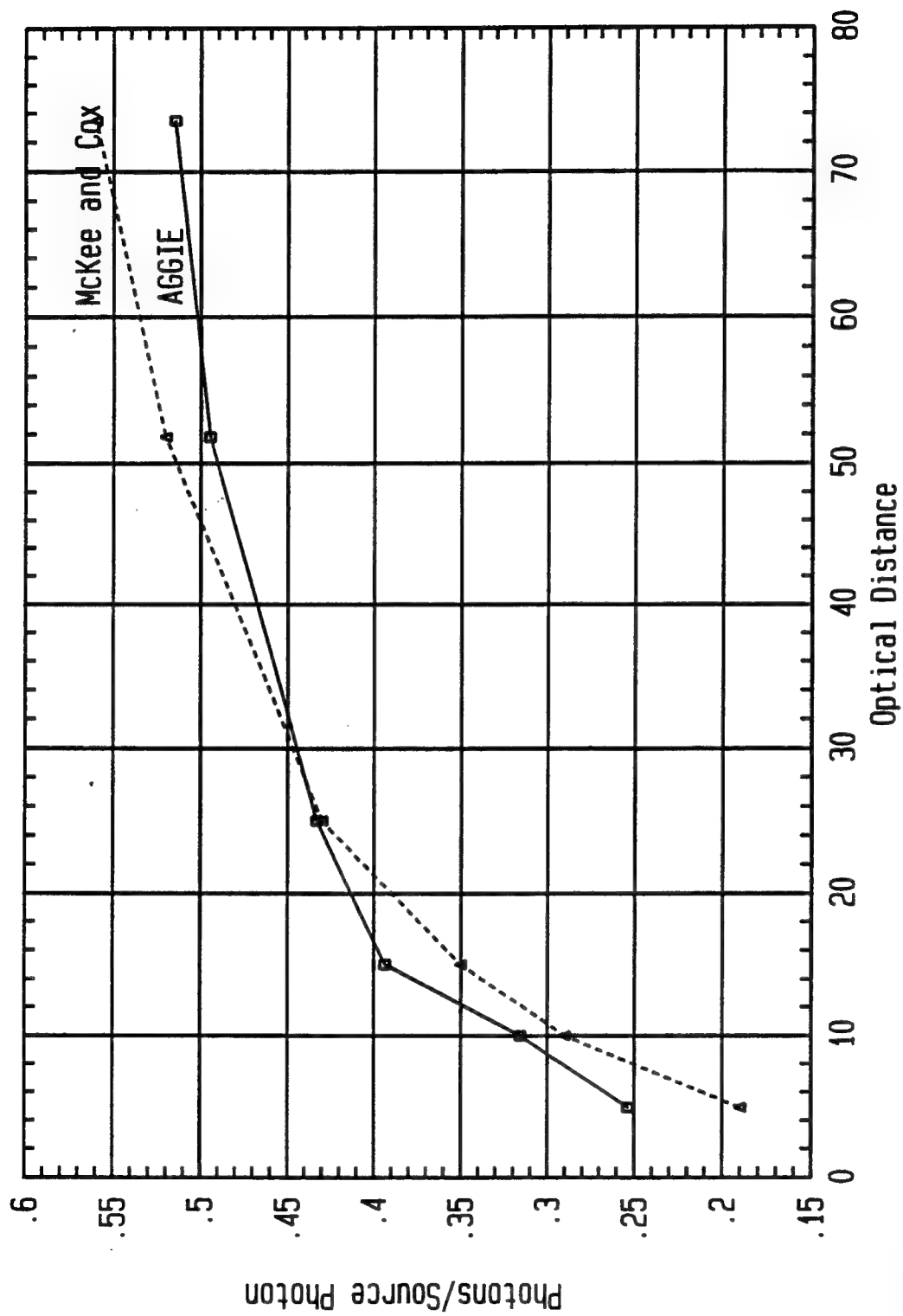


Figure 8. Directional reflectance for zenith angle of 60°.

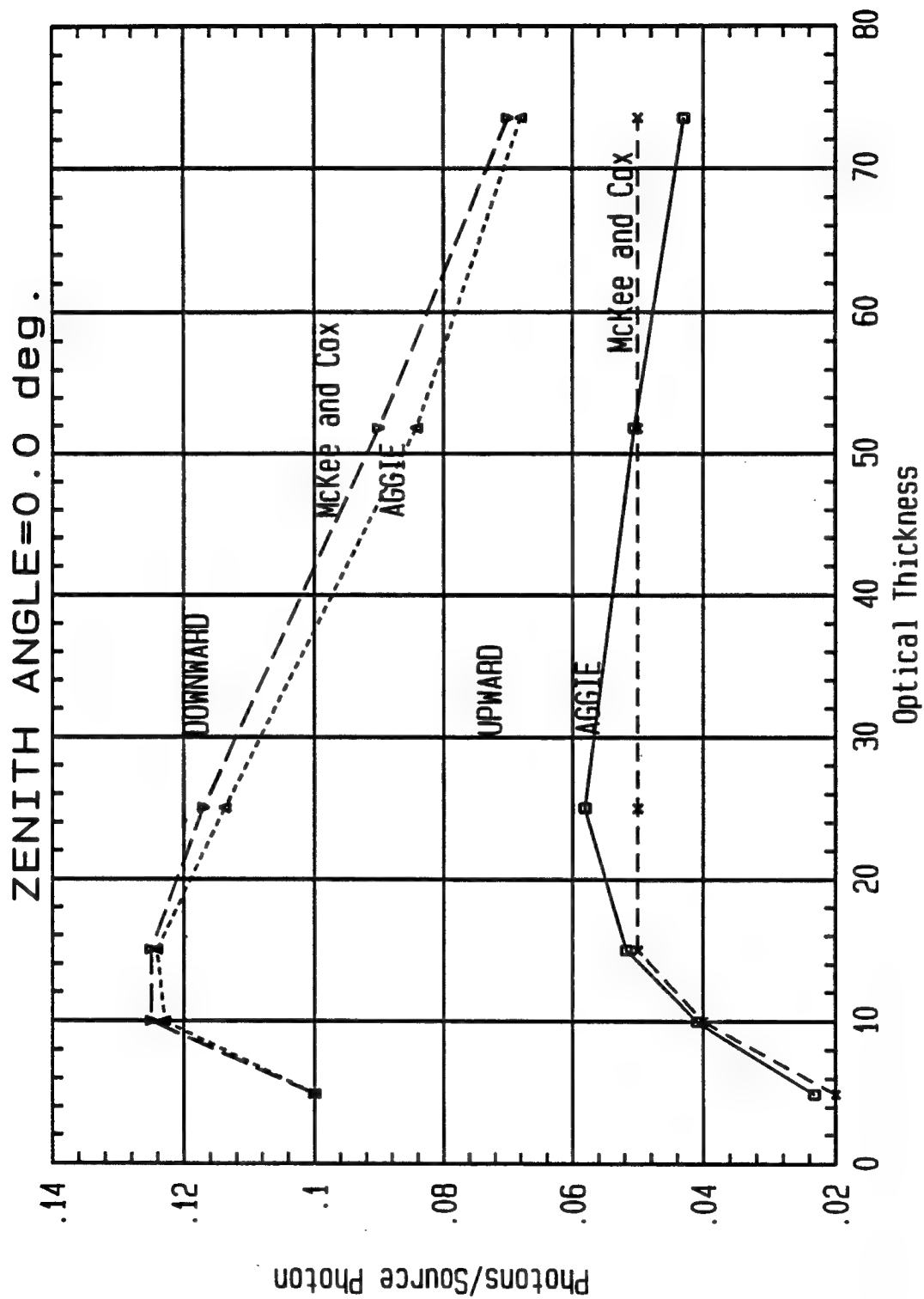


Figure 9. Photons exiting each side of cloud upward and downward: 0.0°.

Similar comparisons of the upward and downward leakages from sides 1, 2, and 3 are shown in figures 10 and 11 for zenith angles of 30° and in figures 12 and 13 for a zenith angle of 60° . Figures 10 and 12 plot the upward exiting photons versus the cloud optical distance. Figures 11 and 13 plot the downward exiting photons. The agreement between the AGGIE data and McKee and Cox data is reasonable except for the downward exiting photons from side 2 when the zenith angle is 30° . The AGGIE data consistently give larger values than the McKee and Cox data when the optical thickness is 25 or less.

The basic difference between McKee and Cox's Monte Carlo code and the AGGIE calculation method is that McKee and Cox scored a photon to be leaking from a side whenever the optical distance to the side was less than the optical distance selected to the next collision. In the AGGIE calculation, the photons were never allowed to escape from the cloud and a history is terminated only when the collision number exceed the maximum allowable or the photon weight fell below the minimum allowable weight. After the AGGIE run, the output collision file was input into the CUBCLD1 code where it was used to estimate the probability of exiting the cloud along the photon's path after collision (or source emission).

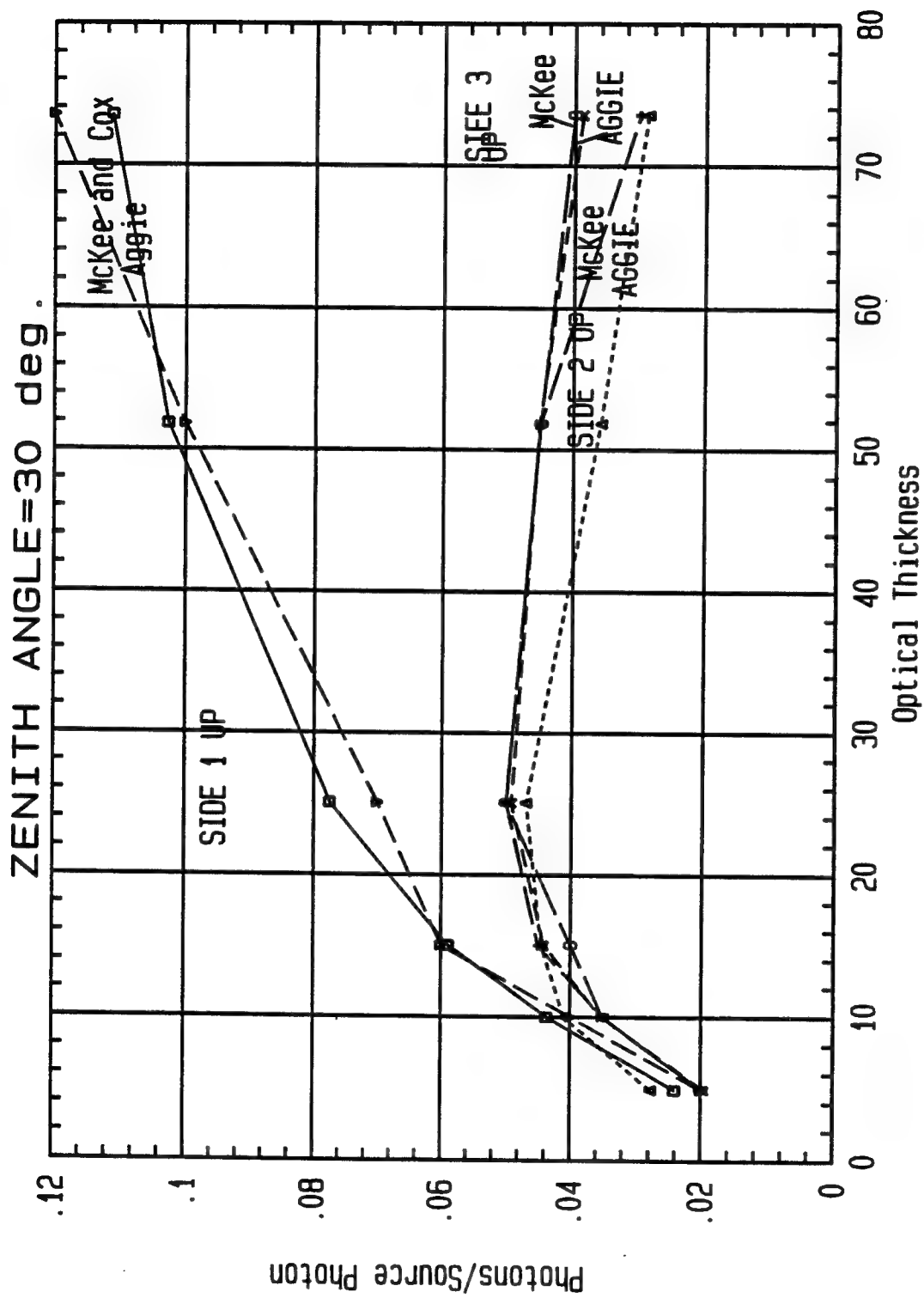


Figure 10. Photons exiting each side of cloud upward: 30°.

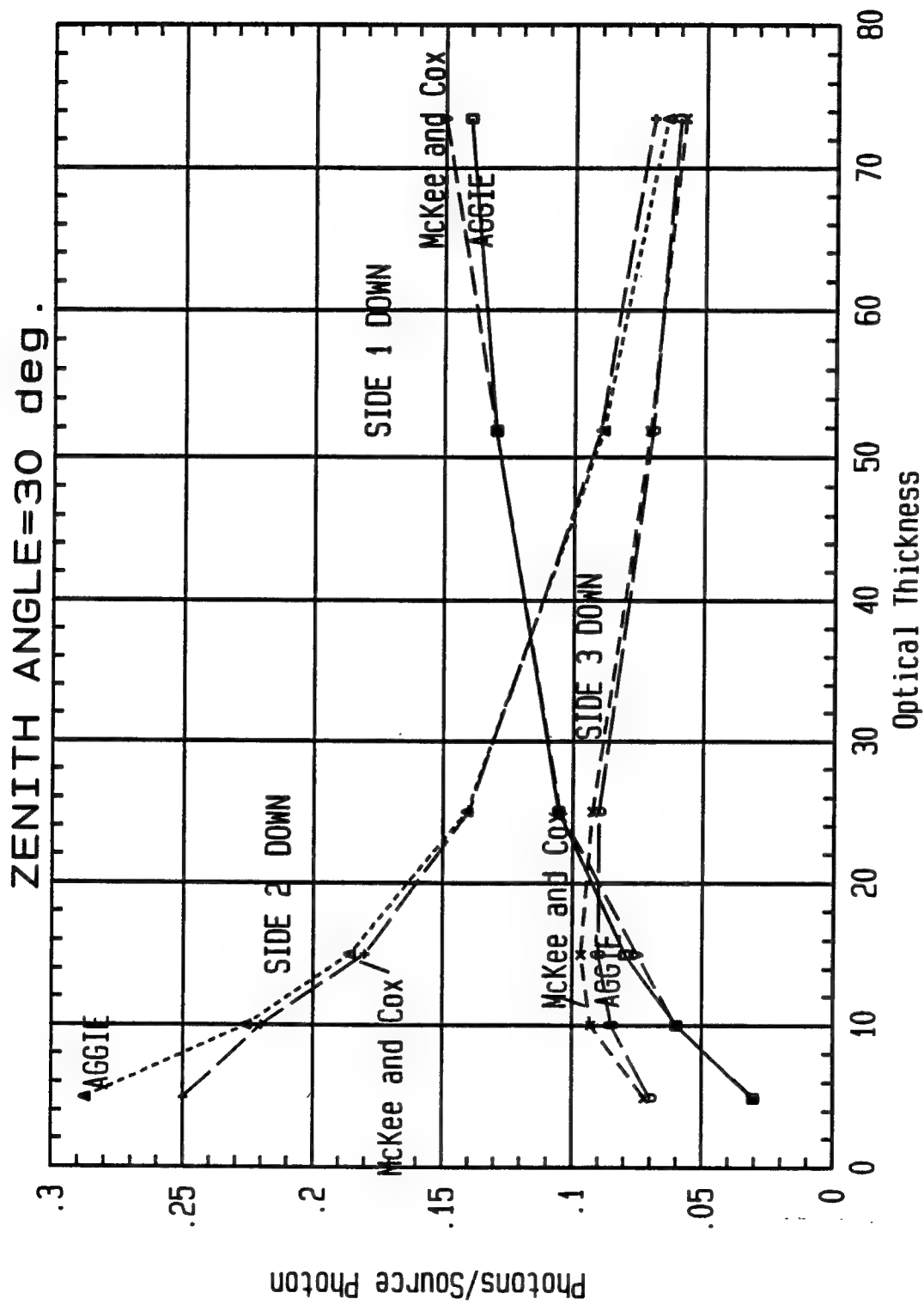


Figure 11. Photons exiting each side of cloud downward: 30°.

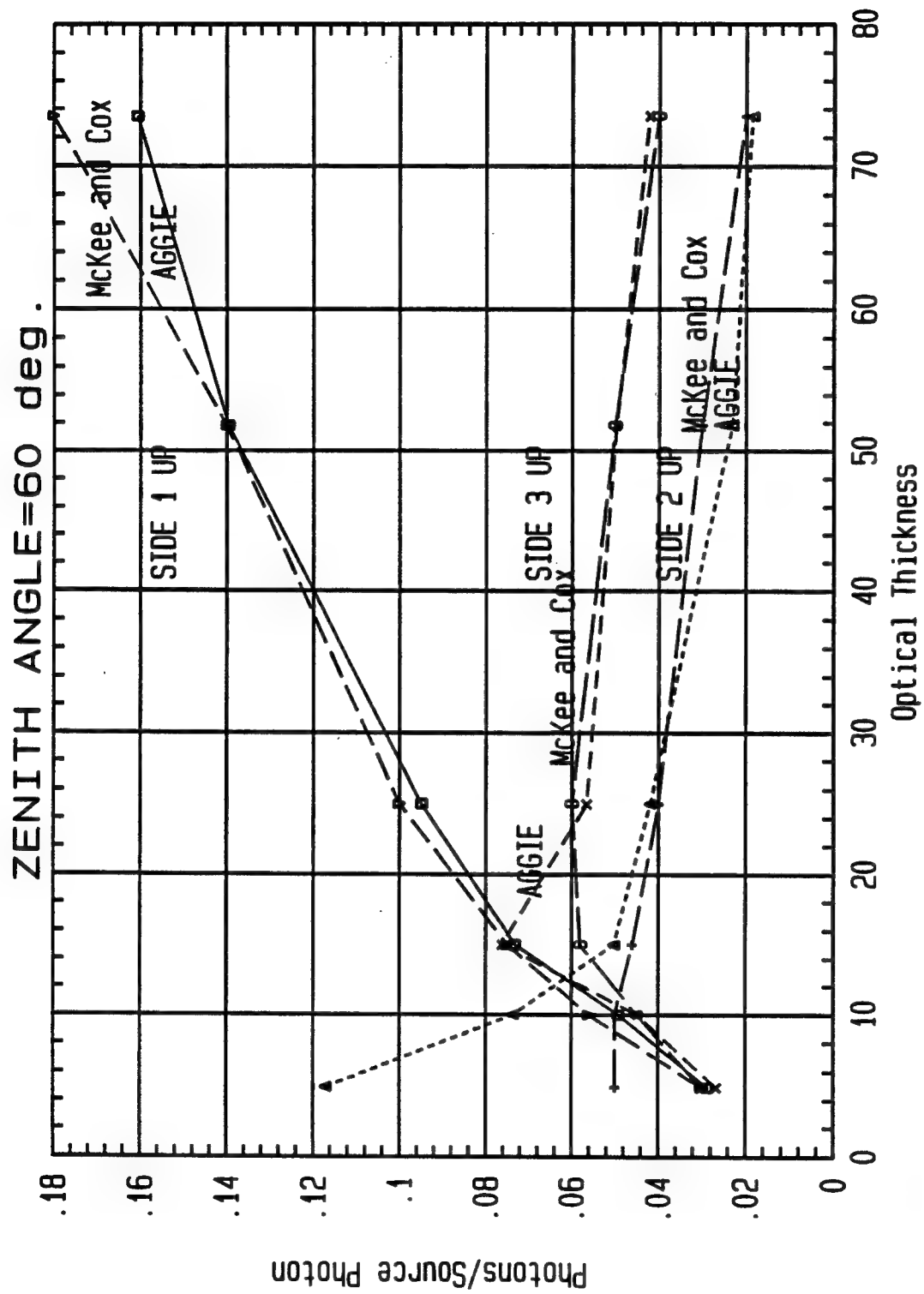


Figure 12. Photons exiting each side of cloud upward: 60°.

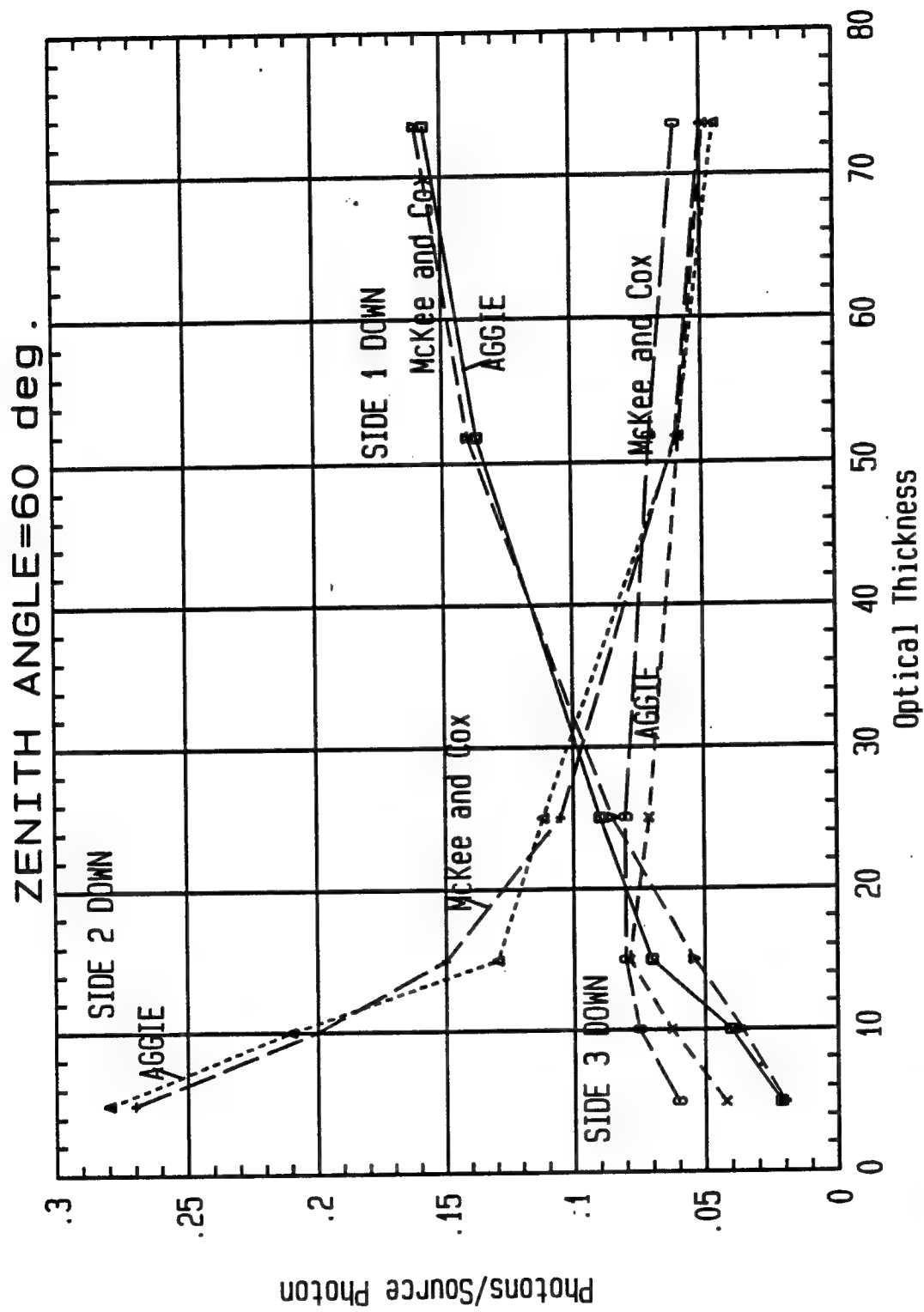


Figure 13. Photons exiting each side of cloud downward: 60°.

Although McKee and Cox estimated the accuracy of their directional reflectance calculations to be 1 to 2 percent for the cloud top and about 5 percent for the cloud sides, no details were given as to how these estimates of accuracy were made. [8] Davies suggests that each photon history can be taken as a Bernoulli trial and his standard deviation results are based on that method. [9] In the CUBCLD1 code used in this study to analyze the collision data files generated by the AGGIE runs, the total number of histories were divided into 10 batches and the mean value for each batch was computed. The standard deviation of the photons leaking out of each side was calculated using the average values for each of the 10 batches. The variance of the photons exiting a given side k is given by the following equation:

$$SDSQ(k) = \frac{1}{N-1} \left(\sum_{i=1}^N x_i^2 - \frac{(\sum_{i=1}^N x_i)^2}{N} \right) \quad (17)$$

where x_i is the average number of photons escaping the k th cloud side for the i th batch and $N = 10$. The standard deviation $SD(k)$ is the square root of $SDSQ(k)$ for the k th side. The percent standard deviations listed in tables 3 through 7 are defined by the following equation:

$$SDEV(K) = \left(\frac{SD(K)}{\left(\frac{SUMTF(K)}{10.0} \right)} \right) * 100 \quad (18)$$

where $SUMTF(k)$ is the total number of photons exiting the cloud through side k in the 10 batches, and $SUMTF(k)/10.0$ is the average number of photons exiting side k . Tables 3 through 7 list the percent standard deviation of the results obtained for the total number of photons leaking out of a given side of the cloud. A discussion of the percent standard deviations computed for each side of the cloud for radiation incident to the top of the cloud and for optical thicknesses of 4.9, 10, 15, 25, 51.8, and 63.5 was given previously.

4. Calculations of Cloud and Ground Emission

The AGGIE Monte Carlo code was used to perform cloud and ground emission calculations for comparison with similar Monte Carlo calculations [10] for a cubical cloud. The cloud was cubical with 1-km-long sides. The optical thickness of the cloud was 10.0 and the single scattering albedo (the ratio of the scattering to total coefficient) was 0.638. In table T.48 of Deirmendjain's book, [16] the cloud phase function for the C.1 water cloud was multiplied by 4π and used to generate the phase function input data needed in AGGIE. The phase function was integrated over the solid angle to obtain the probability distribution for sampling of random scattering angles in AGGIE. The results are shown in figure 14. About 48 percent of the scattering occurs within the first 20° and about 86 percent occurs within the first 40° .

For those problems where the hemispherical power ($\text{W}/\text{m}^2\text{-}\mu\text{m}$) was desired at positions on the top of the cloud, the cloud was defined as a cube having 20 layers parallel to the ground surface, each being 0.05-km thick. The cloud bottom was positioned on the ground. The ground was treated as a surface that did not reflect photons but emitted as a 300-K blackbody. The cloud temperature was 250 K. The ground area for emission was 200-km wide by 200-km long. A 200-km-wide, 200-km-long, and 1.01-km-high parallel-piped region was positioned above the ground. The atmospheric region outside of the cloud consisted of the parallel-piped region minus the cloud. The extinction coefficient in the atmospheric region was $1.0000\text{E-}11$ so that the atmosphere was essentially a void. All the space outside of the ground and the atmosphere region was defined as an external void region.

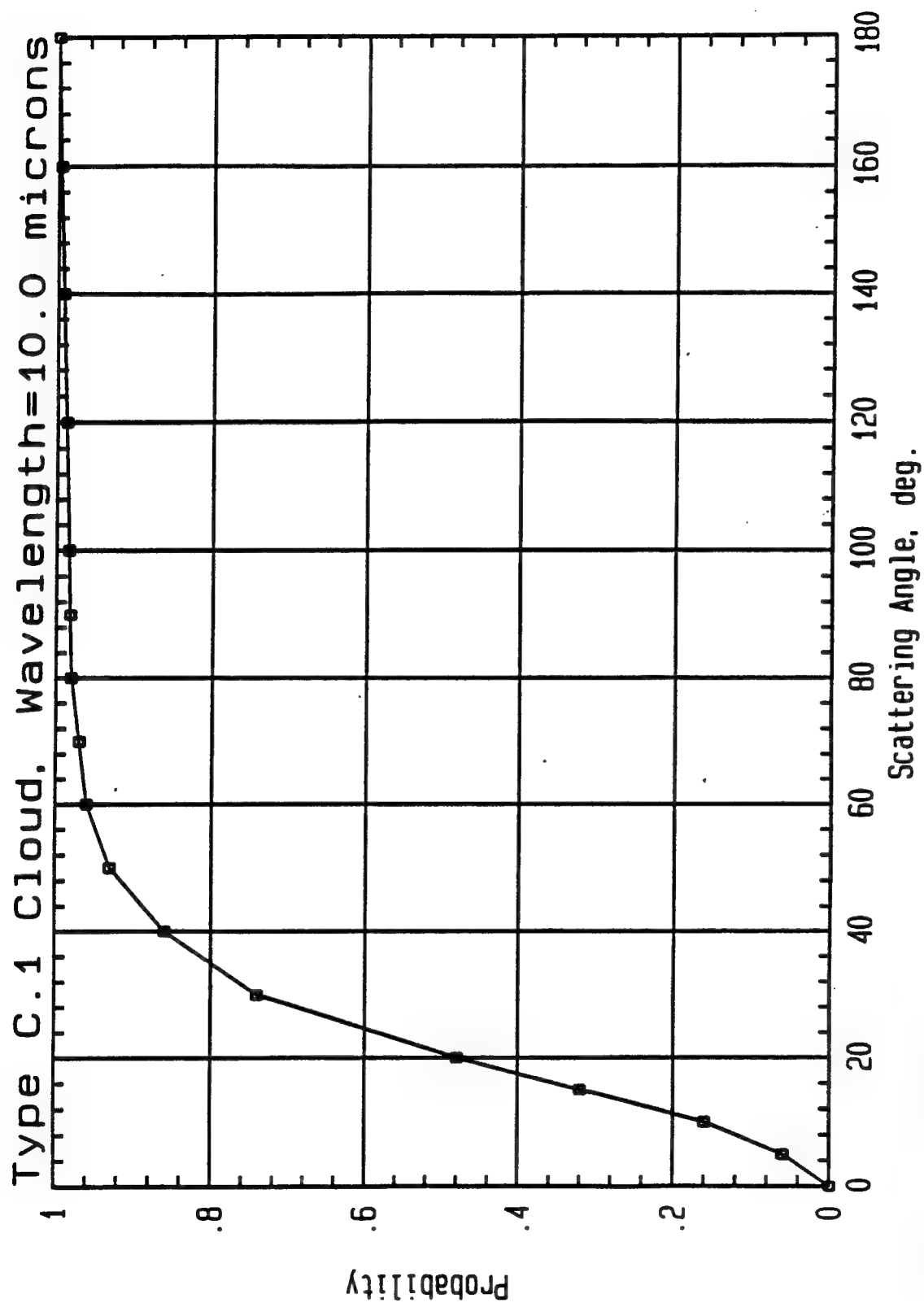


Figure 14. Cumulative probability of photon scatter versus scattering angle.

Two sets of AGGIE problems were run for the above-described geometry. The first set of problems was for a ground emissivity of 0.0 (isolated cloud) and the second set of problems was for a ground emissivity of 1.0 (composite cloud). The origin of the x, y, z coordinate system was at the center of the bottom of the cloud (see figure 1). The top of the cloud was at $z = 1.0$. The x, y, z coordinates of the detector positions on the top of the isolated cloud are shown in table 10. The detector position (0.05, 0.05, 0.99999) is nearest to the center of the top of the cloud. Also shown in table 10 is the hemispheric power ($\text{W/m}^2\text{-}\mu\text{m}$) computed for each of the 15 detector positions and the percent standard deviation of the computed power. The percent standard deviation was computed using the average power determined from each of the 10 batches used in each of the AGGIE runs.

Table 10. Cloud hemispheric power from isolated cloud as seen by detectors on cloud top

Power in $\text{W/m}^2\text{-}\mu\text{m}$					
Detector Position			Emitted Power	BB Temp K	Percent S.D.
X(km)	Y(km)	Z(km)			
.05	.05	.99999	.12490+02	252.17	2.4594
.05	.15	.99999	.12380+02	251.78	2.2567
.15	.15	.99999	.12310+02	251.53	1.2815
.05	.25	.99999	.12100+02	250.78	1.8386
.15	.25	.99999	.12020+02	250.49	.9354
.25	.25	.99999	.11280+02	248.88	1.5472
.05	.35	.99999	.11230+02	247.57	1.6649
.15	.35	.99999	.11040+02	246.85	1.4887
.25	.35	.99999	.10890+02	246.27	2.4179
.35	.35	.99999	.10060+02	242.98	1.8665
.05	.45	.99999	.90400+01	238.68	3.3161
.15	.45	.99999	.89630+01	238.35	2.4122
.25	.45	.99999	.87480+01	237.39	1.7645
.35	.45	.99999	.81700+01	234.75	2.6526
.45	.45	.99999	.67569+01	227.71	4.9874

A FORTRAN code, CLDBATCH, was written to read the AGGIE output file and calculate the percent standard deviation from the batch data. It also created a file that contained the computed power at the detector position, the percent standard deviation, the average power at the detector from each order of collision, the power resulting from emission and scattering in each of the zones defined in the geometry (zone 1 is the ground, zones 2 through 21 are cloud regions, zone 2 is just above the ground, zone 21 is the top layer of the cloud, zone 22 is the atmospheric region, and zone 23 is the outside region), and the effective blackbody temperature at the detector position.

Figure 15 shows plots of the direct and scattered emissions for the isolated cloud from each order of scattering for detector positions 1, 11, and 15 as listed in table 10. The largest component to the total power at the detector is the direct emission by the cloud for the three detector positions on the isolated cloud shown in figure 15. The direct power is 43.636, 46.538, and 50.044 percent of the total power at detector positions 1, 11, and 15, respectively. The sum of the direct and the first three orders of scattering for each of these three detector positions is greater than 98 percent of the total power, indicating that these problems could probably have been evaluated with only five orders of scattering. Figure 15 also shows that the scattered power versus order of scattering is an exponential function (linear on semilog paper).

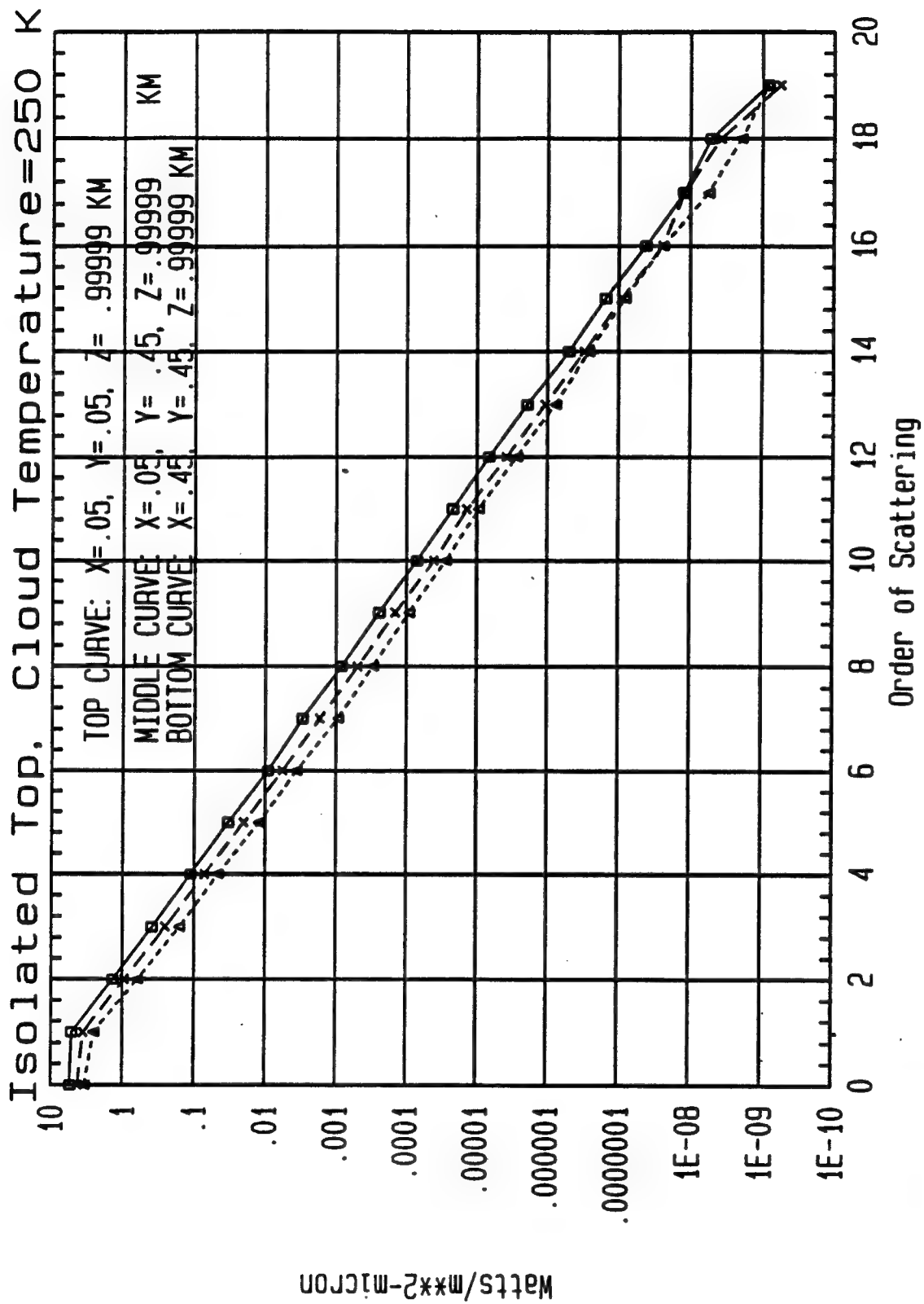


Figure 15. Direct emitted power and emitted power versus order of scattering.

The results of the AGGIE calculations of the emitted power at 15 locations on the top of the composite cloud when the cloud emissivity was 1.0 are shown in table 11. The effective blackbody temperature at each of the 15 detector locations is also shown.

The hemispheric power at the 15 detector locations on top of the composite cloud are all (except for detector position 1) larger than that seen in table 10 for the isolated cloud. A comparison of the hemispherical power at the detector on top of the composite and isolated clouds is shown in table 12. The fourth column lists the power at the detector resulting from ground emission only. The fifth column lists the total power at the detector from the composite cloud. The sixth column lists the cloud-emitted power at the detectors from cloud emission only. The seventh column lists the total hemispheric power as seen by the detectors for the isolated cloud. The hemispheric power from cloud emission only is approximately the same for the composite and isolated clouds. Detector positions 11, 12, 13, 14, and 15 are 0.05 km from the outside edge of the cloud, and therefore, receive more ground emission than the other detector positions. The 7, 8, 9, and 10 detector positions are 0.1 km from the outside edge of the cloud, and therefore, a greater attenuation of the ground emission occurs. From the results for the first detector location shown in table 12, it is doubtful that the ground emission from under the cloud bottom made any contribution to the hemispheric power at the other 14 detector locations. The coordinates of the detector locations are shown in table 10.

For the cases in which the detectors are located on the side of the cloud, the cloud was divided into 20 regions (each 0.05-km thick) and each was perpendicular to the ground and parallel to the side on which the detectors were placed. The ground region and the atmospheric region were the same as for the cloud top calculations. The cloud side containing the detector positions was a y-plane at $y = 0.5$ km. The temperature in the cloud regions was 250 K, and the temperature of the ground was 300 K.

The detector coordinates and the hemispherical power received by detectors placed on side 4 of the cloud are listed in tables 13 and 14 for the isolated and the composite clouds, respectively. A comparison between the cloud emission component of the power at the detector position is listed in table 15 for the

composite and isolated clouds. The components of the hemispheric power at the detector that result only from cloud emission are almost identical in the two cases, which is an indication of the magnitude of the variance of those components.

The cloud emission from the cloud side should be a minimum at detector positions 1, 7, 13, 19, and 25, which are located just above the ground, at detector positions 25, 26, 27, 28, 29, and 30, which are along the edge of the cloud side, and at detector positions 6, 12, 18, 24, and 30, which are located near the top edge of the cloud side where the detectors are located. The maximum cloud emission should occur at detector positions 3, 4, 9, 10, 15, and 16. An examination of the hemispheric emission only from the cloud at each of the 30 detectors positioned on the side located at $y = 0.49999$ km given in table 15 reveals that the maximum and minimum values of the cloud-emitted hemispheric power occurs at those detector locations.

Table 15 shows that the maximum contribution to the detected power by ground emission occurs at detector positions 1, 7, 13, and 19 along the bottom of the cloud side and at detector positions 25, 26, 27, 28, 29, and 30 where ground emission can enter through the y-plane side of the cloud containing the detectors and scatter toward those detector positions. The minimum detector response occurs at detector positions 6, 12, 18, and 24, which are located on the side at 0.05 km below the cloud top. The major part of the ground-emitted power at the detectors comes from photons that underwent a collision inside the cloud and scattered in a direction allowing the photons to exit the cloud side and hit the ground where ground emission occurs. At a given height z above the ground, the ground-emitted power increases with an increase in the x -coordinate. At any x position on the cloud side, the ground emitted power decreases with increasing z .

When the emissivity of the ground is 0.0 for a given x , the cloud emitted power increases as z increases to 0.5 and then decreases with a further increase in z . Similarly, for a given z position, the cloud-emitted power decreases as x increases from 0.0 to 0.5.

Table 11. Cloud hemispheric power from composite cloud as seen by detectors on cloud top

Power in $W/m^2-\mu m$					
Detector Position			Emitted Power	BB Temp K	Percent S.D.
X(km)	Y(km)	Z(km)			
.05	.05	.99999	.12570+02	252.45	1.3732
.05	.15	.99999	.12730+02	253.01	2.2568
.15	.15	.99999	.12800+02	253.25	1.2700
.05	.25	.99999	.13000+02	253.94	1.9341
.15	.25	.99999	.13030+02	254.05	.9563
.25	.25	.99999	.13080+02	254.22	1.3678
.05	.35	.99999	.13770+02	256.54	1.5688
.15	.35	.99999	.13720+02	256.38	1.2867
.25	.35	.99999	.13930+02	257.07	1.2573
.35	.35	.99999	.14700+02	259.55	1.6492
.05	.45	.99999	.16230+02	264.25	2.4233
.15	.45	.99999	.16570+02	265.26	2.1819
.25	.45	.99999	.16530+02	265.14	2.2038
.35	.45	.99999	.17080+02	266.74	1.2490
.45	.45	.99999	.19000+02	272.09	2.2595

Table 12. Comparison of hemispheric power at detectors on top of composite and isolated clouds

			Power in W/m ² -μm			
Detector Position			Composite Cloud		Cloud Power	Isolated Cloud Power
X(km)	Y(km)	Z(km)	Ground Power	Cloud & Ground Power		
.05	.05	.99999	.0000+00	.1257+02	.1257+02	.1249+02
.05	.15	.99999	.3481+00	.1273+02	.1238+02	.1238+02
.15	.15	.99999	.4972+00	.1280+02	.1230+02	.1231+02
.05	.25	.99999	.9003+00	.1300+02	.1210+02	.1210+02
.15	.25	.99999	.1016+01	.1303+02	.1158+02	.1158+02
.25	.25	.99999	.1500+01	.1308+02	.1158+02	.1158+02
.05	.35	.99999	.2543+01	.1377+02	.1123+02	.1123+02
.15	.35	.99999	.2685+01	.1372+02	.1103+02	.1104+02
.25	.35	.99999	.3039+01	.1393+02	.1089+02	.1089+02
.35	.35	.99999	.4644+01	.1470+02	.1006+02	.1006+02
.05	.45	.99999	.7192+01	.1623+02	.9038+01	.9040+01
.15	.45	.99999	.7609+01	.1657+02	.8961+01	.8963+01
.25	.45	.99999	.7789+01	.1653+02	.8743+01	.8748+01
.35	.45	.99999	.8906+01	.1708+02	.8174+01	.8170+01
.45	.45	.99999	.1225+02	.1900+02	.6750+01	.6750+01

Table 13. Cloud hemispheric power from isolated cloud as seen by detectors on cloud side.

Power in W/m ² -μm					
Detector Position			Emitted Power	BB Temp K	Percent S.D.
X(km)	Y(km)	Z(km)			
.05	.49999	.08333	.10020+02	242.82	2.6357
.05	.49999	.25000	.12200+02	251.14	2.2169
.05	.49999	.41667	.12700+02	252.91	1.5548
.05	.49999	.58333	.12390+02	251.82	1.7840
.05	.49999	.75000	.11980+02	250.35	2.7580
.05	.49999	.91667	.10170+02	243.43	1.4987
.15	.49999	.08333	.99700+01	242.62	2.0365
.15	.49999	.25000	.11950+02	250.24	1.7374
.15	.49999	.41667	.12440+02	251.99	2.2473
.15	.49999	.58333	.12470+02	252.10	1.6951
.15	.49999	.75000	.11960+01	250.27	1.5359
.15	.49999	.91667	.99120+01	242.38	2.0969
.25	.49999	.08333	.97650+01	241.77	3.8058
.25	.49999	.25000	.11560+02	248.81	2.3009
.25	.49999	.41667	.12020+02	250.49	1.7696
.25	.49999	.58333	.12100+02	250.78	2.3567
.25	.49999	.75000	.11630+02	249.07	1.4525
.25	.49999	.91667	.97700+01	241.79	2.3704
.35	.49999	.08333	.91910+01	239.34	2.9903
.35	.49999	.25000	.10840+02	246.08	1.9340
.35	.49999	.41667	.11200+02	247.46	1.9511
.35	.49999	.58333	.11310+02	247.87	2.2898
.35	.49999	.75000	.10830+02	246.04	2.0902
.35	.49999	.91667	.89660+01	238.36	1.5211
.45	.49999	.08333	.73000+01	230.53	2.2336
.45	.49999	.25000	.87650+01	237.47	1.9554
.45	.49999	.41667	.90710+01	238.82	2.4233
.45	.49999	.58333	.91770+01	239.28	2.0215
.45	.49999	.75000	.87310+01	237.32	1.9765
.45	.49999	.91667	.74230+01	231.14	3.5569

Table 14. Cloud hemispheric power from composite cloud as seen by detectors on cloud side

Power in W/m ² -μm					
Detector Position			Emitted Power	BB Temp K	Percent S.D.
X(km)	Y(km)	Z(km)			
.05	.49999	.08333	.16440+02	264.88	1.8033
.05	.49999	.25000	.14070+02	257.53	2.4125
.05	.49999	.41667	.14530+02	259.01	1.3777
.05	.49999	.58333	.14180+02	257.89	2.0506
.05	.49999	.75000	.13650+02	256.14	2.8465
.05	.49999	.91667	.11720+02	249.40	1.7802
.15	.49999	.08333	.16260+02	264.34	1.5991
.15	.49999	.25000	.13830+02	256.74	1.8233
.15	.49999	.41667	.14310+02	258.31	1.8972
.15	.49999	.58333	.14160+02	257.82	1.8760
.15	.49999	.75000	.13830+02	256.74	2.2973
.15	.49999	.91667	.11630+02	249.07	2.5559
.25	.49999	.08333	.16290+02	264.43	2.7573
.25	.49999	.25000	.14290+02	258.24	1.8457
.25	.49999	.41667	.14230+02	258.05	1.6653
.25	.49999	.58333	.14060+02	257.49	2.5045
.25	.49999	.75000	.14060+02	257.49	2.5045
.25	.49999	.91667	.13620+02	256.04	1.4177
.35	.49999	.08333	.11690+02	249.29	2.2454
.35	.49999	.25000	.15680+02	262.60	2.3291
.35	.49999	.41667	.14460+02	258.79	1.1880
.35	.49999	.58333	.14460+02	258.79	1.1888
.35	.49999	.75000	.14200+02	257.95	1.8990
.35	.49999	.91667	.14210+02	257.98	2.1485
.45	.49999	.08333	.13720+02	256.38	3.0084
.45	.49999	.25000	.11820+02	249.76	1.9101
.45	.49999	.41667	.13700+02	256.31	2.7436
.45	.49999	.58333	.14700+02	259.55	2.4437
.45	.49999	.75000	.14260+02	258.14	3.0865
.45	.49999	.91667	.14260+02	258.14	2.2647

Table 15. Comparison of hemispheric power at detectors on side of composite and isolated clouds

			Power in W/m ² -μm			
Detector Position			Composite Cloud		Cloud Power	Isolated Cloud Power
X (km)	Y(km)	Z(km)	Ground Power	Cloud & Ground Power		
.05	.49999	.08333	.6421+01	.1644+02	.1002+02	.1002+02
.05	.49999	.25000	.1865+01	.1407+02	.1221+02	.1220+02
.05	.49999	.41667	.1824+01	.1453+02	.1271+02	.1270+02
.05	.49999	.58333	.1792+01	.1418+02	.1239+02	.1239+02
.05	.49999	.75000	.1675+01	.1365+02	.1198+02	.1198+02
.05	.49999	.91667	.1557+01	.1172+02	.1016+02	.1017+02
.15	.49999	.08333	.6292+01	.1626+02	.9968+01	.9970+02
.15	.49999	.25000	.1873+01	.1383+02	.1196+02	.1195+02
.15	.49999	.41667	.1875+01	.1431+02	.1244+02	.1244+02
.15	.49999	.58333	.1690+01	.1416+02	.1247+02	.1247+02
.15	.49999	.75000	.1869+01	.1383+02	.1196+02	.1196+02
.15	.49999	.91667	.1716+01	.1163+02	.9914+01	.9912+01
.25	.49999	.08333	.6523+01	.1629+02	.9767+01	.9765+01
.25	.49999	.25000	.2737+01	.1429+02	.1155+02	.1156+02
.25	.49999	.41667	.2208+01	.1423+02	.1202+02	.1202+02
.25	.49999	.58333	.1956+01	.1406+02	.1210+02	.1210+02
.25	.49999	.75000	.1987+01	.1362+02	.1163+02	.1163+02
.25	.49999	.91667	.1920+01	.1169+02	.9770+01	.9770+01
.35	.49999	.08333	.6489+01	.1568+02	.9191+01	.9191+01
.35	.49999	.25000	.3616+01	.1446+02	.1084+02	.1084+02
.35	.49999	.41667	.2994+01	.1420+02	.1121+02	.1120+02
.35	.49999	.58333	.2901+01	.1421+02	.1131+02	.1131+02
.35	.49999	.75000	.2895+01	.1372+02	.1083+02	.1083+02
.35	.49999	.91667	.2857+01	.1182+02	.8963+01	.8966+01
.45	.49999	.08333	.6402+01	.1370+02	.7298+01	.7300+01
.45	.49999	.25000	.5931+01	.1470+02	.8769+01	.8765+01
.45	.49999	.41667	.5185+01	.1426+02	.9075+01	.9071+01
.45	.49999	.58333	.5084+01	.1426+02	.9176+01	.9177+01
.45	.49999	.75000	.5100+01	.1382+02	.8730+01	.8731+01
.45	.49999	.91667	.5082+01	.1250+02	.7418+01	.7423+01

4.1 Validation of the Monte Carlo Calculations of Hemispherical Power Emitted from the Top and Side of a Cubical Cloud

Harshvardhan, Weinmann, and Davies [10] have reported the results of Monte Carlo calculations of the emitted hemispherical power escaping from the top and sides of a cubical cloud with an optical thickness of 10 for a wavelength of 10 μm . Figure 16 shows a comparison between the results of AGGIE calculations of the hemispherical power at detectors on the top of the cloud and the data from Harshvardhan et al. when the emissivity of the ground was taken to be 0.0 (isolated top). The upper number in each box is the effective blackbody temperature obtained from the AGGIE calculations and the lower number in each box is the effective blackbody temperature obtained from Harshvardhan et al.

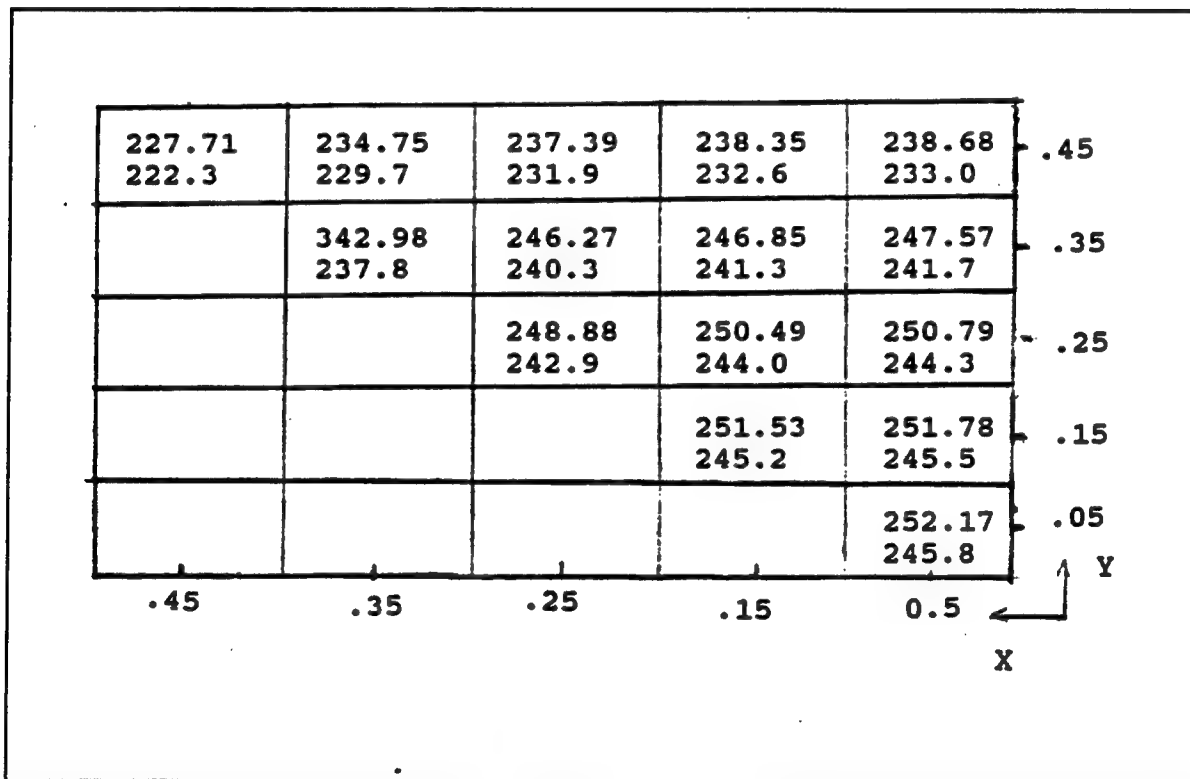


Figure 16. Effective blackbody temperature for upward hemispheric power at top of isolated cloud.

For the isolated cloud case, the AGGIE calculations were between 5° to 6.5° higher in the effective blackbody temperature than the data from Harshvardhan et al. Converting the effective blackbody temperatures for the isolated cloud case in Harshvardhan et al. to hemispheric power in $\text{W/m}^2\text{-}\mu\text{m}$ showed that the differences between the AGGIE calculated power and Harshvardhan et al. calculated power is between 12.14 and 14.27 percent of the AGGIE calculated powers, with the AGGIE data being higher than the data from Harshvardhan et al.

Figure 17 shows a comparison of the results of the AGGIE calculations of the hemispherical power at detectors on the top of the cloud, when the ground emissivity is 1.0 (composite cloud) and data for the same case from Harshvardhan et al. The upper number in each box is the AGGIE calculated effective blackbody temperature, and the lower number in each box is the effective blackbody temperature from Harshvardhan et al.

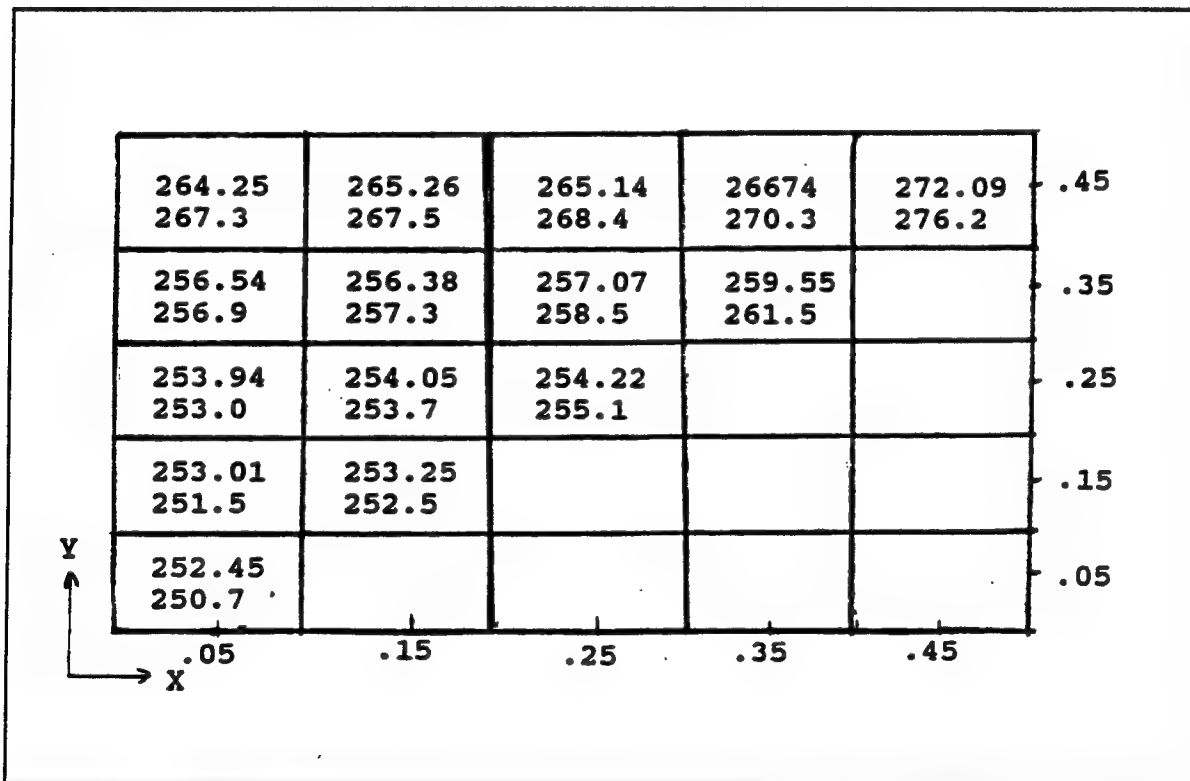


Figure 17. Effective blackbody temperature for upward hemispheric power at top of composite cloud.

For the composite cloud case, the differences between the AGGIE calculated power and the powers computed from the effective blackbody temperatures reported in Harshvardhan et al. were between 8.23 and 0.78 percent of the AGGIE calculated power. For 10 of the cases, the data from Harshvardhan et al. calculated power was greater than the AGGIE calculated power. For the other five cases, the AGGIE calculated power was up to 4.23 percent higher than data from Harshvardhan et al. The AGGIE results for the cloud emitted power was 12.57 to 14.27 percent higher in all cases than similar data from Harshvardhan et al. This indicated that AGGIE is computing more cloud-scattered power at the detectors than shown by the Harshvardhan et al. data. The data from Harshvardhan et al. for ground emission is higher than that computed by AGGIE by up to 8.23 percent. The source simulation characteristics shown in table 1 from Harshvardhan et al. indicate that separate Monte Carlo calculations were made to determine the power at the detector from cloud emission, the power at the detector from emission by the ground under the cloud, and emission from the ground that enters the sides of the cloud. The AGGIE code computes the emitted power from each of these components, depending only on the photon paths selected from the detector position. The detector in AGGIE is a unit area detector and the detector in the Monte Carlo calculations described in McKee and Cox [8] was a larger area detector. Considering the differences in the type of detector used in the calculations, it appears that the two different calculational methods are yielding approximately the same results within a reasonable variance.

After the AGGIE calculations of the hemispheric power at the detectors on the cloud side were run, it was discovered that the data from Harshvardhan et al. were for the effective blackbody temperature of the upward-emerging hemispheric power. If the isolated cloud case is assumed to have that one-half of the power emerging from a side in the upward direction and one-half is in the downward direction, then the effective hemispheric blackbody temperature at a given detector position on the cloud side would be that listed in table 13. A comparison is made in figure 18 of the AGGIE hemispheric power calculations at each detector position with the data reported by Harshvardhan et al. The difference between the AGGIE effective temperature and the effective temperatures from Harshvardhan et al. divided by the AGGIE effective temperature (times 100) for each detector position is a measure of the

difference in the two differently-calculated effective temperatures. The results of the calculation for each detector position shows that the data from Harshvardhan et al. differed from the AGGIE data by 0.72 percent to as much as 7.22 percent for all the 30 detector positions on the cloud side. The percentage difference was highest for sensors located 0.05 km above the ground, and the percentage difference decreased as the detector z coordinate was increased.

243.43 245.6	242.38 245.0	241.79 243.9	238.36 241.2	231.14 232.8	.91667
250.35 246.4	250.27 246.1	249.07 244.8	246.04 241.9	237.32 233.5	.75
251.82 246.1	252.10 245.9	250.78 244.6	247.87 241.9	239.28 233.3	.58333
252.91 245.2	251.99 245.0	250.49 243.8	247.46 241.1	238.82 232.6	.41667
251.14 241.7	250.24 241.7	248.81 240.9	246.08 238.4	237.47 230.2	.250
242.82 225.3	242.62 225.1	241.77 224.5	239.34 223.1	230.53 216.5	.0833
.05	.15	.25	.35	.45	

Figure 18. Effective blackbody temperature for upward hemispheric power exiting side of isolated cloud.

If one-half of the hemispheric power emerging from a given location on the cloud side is assumed to be moving in the upward direction, then figure 19 shows the effective blackbody temperature given by the AGGIE calculation and by the data from Harshvardhan et al. for the composite cloud. The effective temperature given by the data from Harshvardhan et al. in figure 19 differs from the results given by the AGGIE calculation from 0.20 percent to as much as 9.27 percent, depending on the detector position on the cloud side. The

largest differences occurred at the detector positioned at 0.05 km above the ground surface. The percentage difference varied from 4.16 to 9.27 as the detector position moved from near the perpendicular centerline of the cloud side to near the cloud edge. The percent difference between the AGGIE data and the data from Harshvardhan et al. varied from 3.97 to 9.27 percent for detectors positioned 0.5 km from the edge of the cloud side.

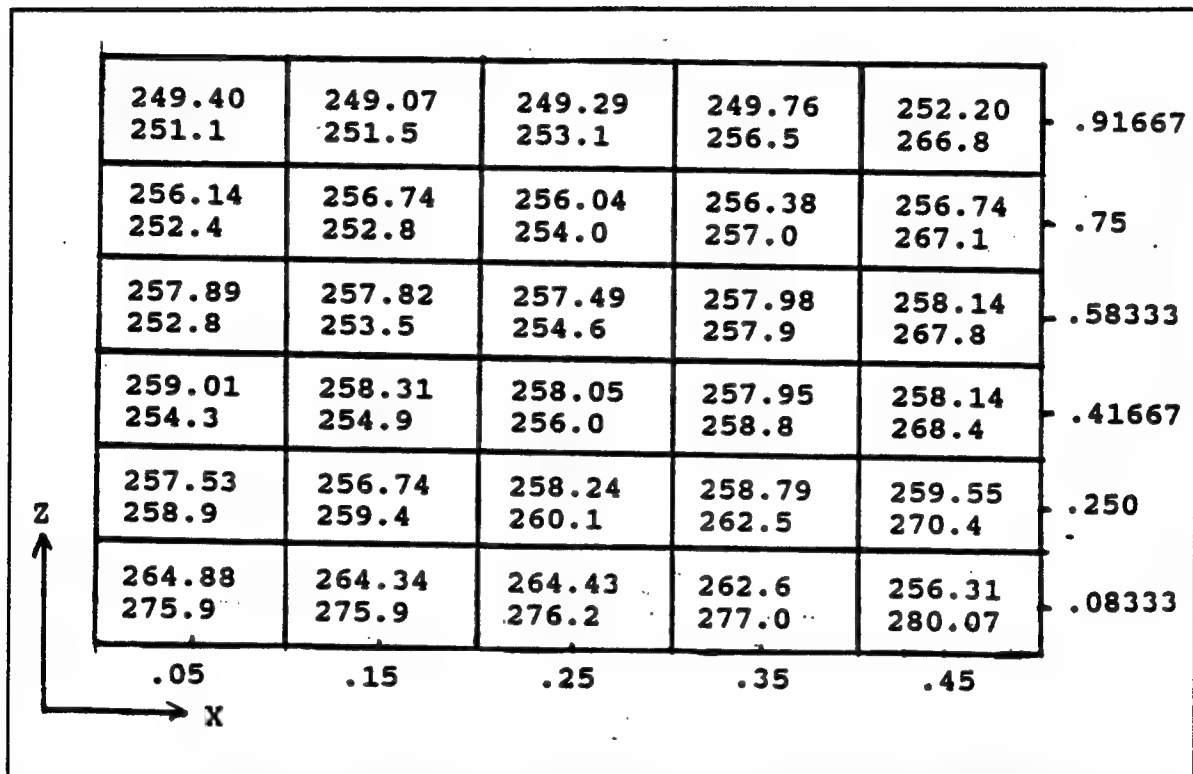


Figure 19. Effective blackbody temperature for upward hemispheric power exiting side of composite cloud.

If one-half of the cloud-emitted radiation is assumed to leave the cloud side at a given detector location in the upward direction and all of the ground-produced radiation is assumed to leave the side in the upward direction, the upward-leaking emitted radiation is given as

$$UPRADIATION = 0.5 \left(\frac{(TOTAL - GROUND)}{2.0} \right) + GROUND \quad (19)$$

where TOTAL is the total hemispheric radiation at the detector and GROUND is the portion of the total resulting from ground emission. The effective temperature is the effective temperature for 2.0 X UPRADIATION. Figure 20 shows a comparison of the modified AGGIE results with the data from Harshvardhan et al. for the composite cloud and the detectors positioned on a cloud side. The percent difference between the modified AGGIE results and the data from Harshvardhan et al. varies from 1.15 to 3.98 percent of the modified AGGIE results.

It appears that the differences between the AGGIE calculations for the isolated cloud and for the composite cloud are small enough that it can be said that the two different calculations are in good agreement.

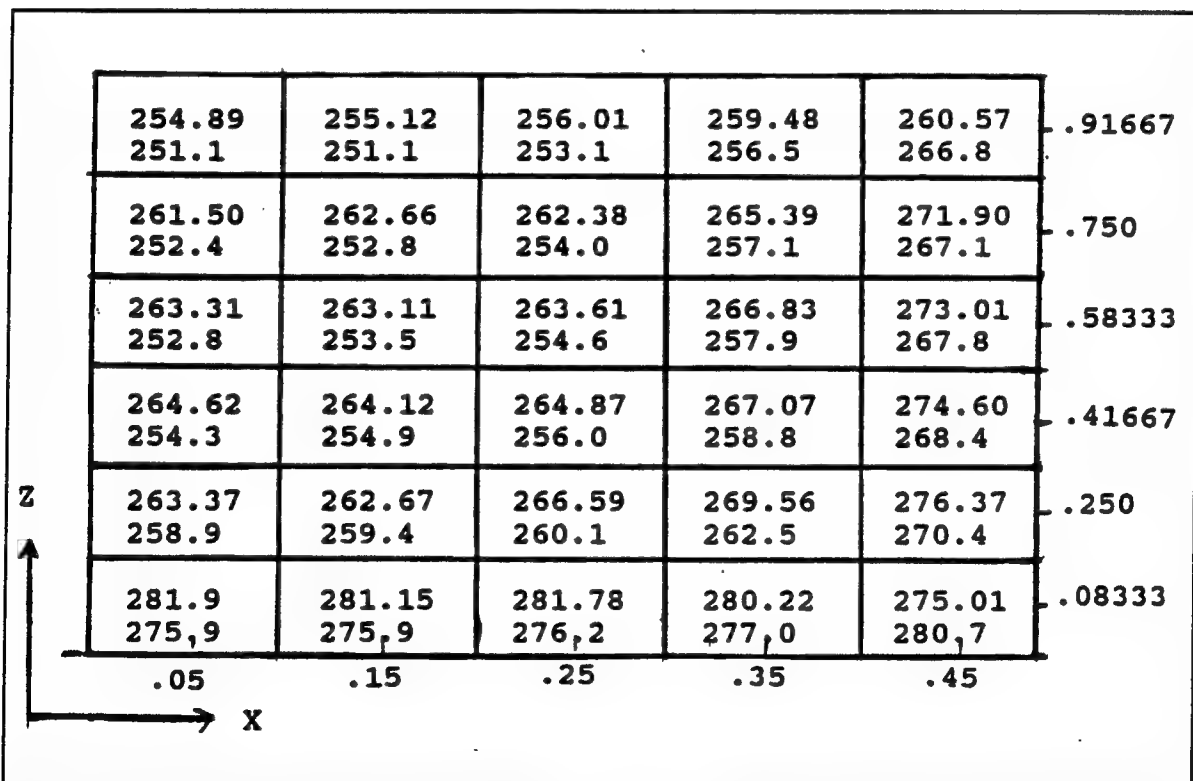


Figure 20. Effective blackbody temperature for the upward hemispheric power exiting the composite cloud side: Modified AGGIE data.

5. Conclusions and Recommendations

The AGGIE code was modified to efficiently compute the polar and azimuthal angle distributions of photons leaking out of each side of a box-shaped cloud. Changes were also made to AGGIE so that it could calculate monochromatic hemispheric blackbody radiation escaping at different locations on the sides of a box-shaped cloud when the cloud and the ground are both emitting blackbodies.

The modified AGGIE code was validated by comparison with the Monte Carlo results of McKee and Cox [8] for the fraction of the incident radiation escaping through the six sides of a cubic cloud when solar radiation is incident to both the top and a side of the cloud for cloud optical thickness between 4.9 and 73.5. AGGIE was also validated for calculations of thermal emission from box-shaped clouds through comparison with Harshvardhan, Weinmann, and Davies [10] calculations for the upwelling hemispheric power escaping from the cloud top and one of the cloud sides.

To validate the BLIRB model, it is recommended that further AGGIE calculations should be run for comparison with BLIRB results for multiple cloud scenarios. The BLIRB calculations should be run for sunlight and thermal emission sources. Although AGGIE can treat multiple cloud sources, the CUBCLD1 code should be modified to include multiple cloud problems. The AGGIE code can compute hemispheric thermal radiation power at a detector location where radiation from other clouds can contribute to the thermal radiation at the detector location. It is suggested that AGGIE be modified to give the polar and azimuthal angle distribution of the hemispheric power emerging from the cloud at a detector position.

References

1. Guinn, J. A. Jr., and D. G. Collins, "AGGIE, A Generalized Geometry Monte Carlo Program for Simulating the Scattering of Laser Light," Radiation Research Associates, Inc., Technical Report RRA-T7813, October 1978.
2. Blattner, W. G., and D. G. Leggett, "Utilization Instructions for the AGGIE-2 Monte Carlo Code," Radiation Research Associates, Inc., Research Note RRA-N8602, June 1986.
3. Andrews, M. C., and D. G. Leggett, "AGGIE3 Technical Report on a Generalized Geometry Irradiance Estimator Monte Carlo Program," Radiation Research Associates, Inc., Technical Report RRA-T8901, May 1989.
4. Wells, M. B., "The AGGIE-4 Monte Carlo Procedure," Radiation Research Associates, Inc., Technical Report RRA-T9001, February 1990.
5. Andrews, M. C., and D. G. Leggett, "Utilization Instructions for the AGGIE-4 and ANACOL Computer Codes," Radiation Research Associates, Inc., Research Note RRA-N9001, February 1990.
6. Zardecki, A., "Radiative Transfer in Three Dimension," Technical Report Prepared under Delivery Order No. 0541, TCN Number 92-480 for Contract No. DAAL03-91-C-0034, June 1993.
7. Zardecki, A., "Three Dimensional Extension of Boundary Layer Illumination Radiation Balance Model for Imaging Application," Los Alamos Consulting, Technical Report Prepared under Delivery Order No. 0541, TCN Number 92-480 for Contract No. DAAL03-91-C-0034, December 1993.
8. McKee, T. B., and S. K. Cox, "Scattering of Visible Radiation by Finite Clouds," *Journal of the Atmospheric Sciences* **31**, pp. 1885-1892, 1974.
9. Davies, R., "The Effect of Finite Geometry on the Three Dimensional Transfer of Solar Irradiance in Clouds," *Journal of Atmospheric Physics* **35**, pp. 1712-1725, 1978.

10. Harshvardhan, J., A. Weinmann, and R. Davies, "Transport of Infrared Radiation in Cuboidal Clouds," *Journal of Atmospheric Sciences* **38**, pp. 2500-2512, 1982.
11. Blattner, W. G. M., "Utilization Instructions for Operation of the TPART-III Program," Radiation Research Associates, Inc., Research Note RRA-N7709, 1977.
12. Blattner, W. G. M., D. G. Collins, and M. B. Wells, "Computer Procedures for Calculating Light Scattering from Lasers," Radiation Research Associates, Inc., Technical Report RRA-T7708, 1977.
13. "MORSE-CG, General Purpose Monte Carlo Multigroup Neutron and Gamma-Ray Transport Code with Combinatorial Geometry," RSIC Computer Code Collection CCC-203, Oak Ridge National Laboratory, 1976.
14. Hayes, C. H., and W. C. Reeves, "A Track Dust Model for Battlefield Environments," U.S. Army Missile Research and Development Command, Technical Report T-CR-79-11, 1979.
15. Schutt, A. M., and C. H. Hayes, "A High-Explosive Dust Model for Battlefield Environments," U.S. Army Missile Research and Development Command, Technical Report T-CR-79-10, 1979.
16. Deirmendjian, D., "Electromagnetic Scattering on Spherical Polydispersions," American Elsevier Publishing Company, Inc., New York, 1969.

Acronyms and Abbreviations

AGGIE A Generalized Geometry Irradiance Estimator

BLIRB Boundary Layer Illumination Radiation Balance Model

CG combinatorial-geometry

Distribution

Copies

ARMY CHEMICAL SCHOOL
ATTN ATZN CM CC MR BARNES
FT MCCLELLAN AL 36205-5020

1

NASA MARSHAL SPACE FLT CTR
SPACE SCIENCE LABORATORY
ATMOSPHERIC SCIENCES DIVISION
ATTN E501 DR FICHTL
HUNTSVILLE AL 35802

1

NASA MARSHALL SPACE FLT CTR
ATMOSPHERIC SCIENCES DIVISION
ATTN CODE ED 41
HUNTSVILLE AL 35812

1

ARMY STRATEGIC DEFENSE COMMAND
ATTN CSSD SL L DR LILLY
PO BOX 1500
HUNTSVILLE AL 35807-3801

1

ARMY MISSILE COMMAND
ATTN AMSMI RD AC AD DR PETERSON
RSA AL 35898-5242

1

ARMY MISSILE COMMAND
ATTN AMSMI RD DE SE MR LILL JR
RSA AL 35898-5245

1

ARMY MISSILE COMMAND
ATTN AMSMI RD AS SS MR ANDERSON
RSA AL 35898-5253

1

ARMY MISSILE COMMAND
ATTN AMSMI RD AS SS MR B WILLIAMS 1
RSA AL 35898-5253

ARMY MISSILE COMMAND
REDSTONE SCIENTIFIC INFORMATION CTR
ATTN AMSMI RD CS R DOCUMENTS 1
RSA AL 35898-5241

ARMY AVIATION CTR
ATTN ATZQ D MA MR HEATH 1
FT RUCKER AL 36362

ARMY INTELLIGENCE CTR FT HUACHUCA
ATTN ATSI CDC C MR COLANTO 1
FT HUACHUCA AZ 85613-7000

NORTHROP CORPORATION
ELECTRONICS SYSTEMS DIVISION
ATTN DR TOOLEY 1
2301 WEST 120TH STREET BOX 5032
HAWTHORNE CA 90251-5032

PACIFIC MISSILE TEST CTR GEOPHYSICS DIVISION
ATTN CODE 3250 MR BATTALINO 1
POINT MUGU CA 93042-5000

CODE 3331
NAVAL WEAPONS CTR
ATTN DR SHLANTA 1
CHINA LAKE CA 93555

LOCKHEED MISSILES & SPACE CO INC
KENNETH R HARDY
ORG 91 01 B 255
3251 HANOVER STREET
PALO ALTO CA 94304-1191

1

NAVAL OCEAN SYSTEMS CTR
ATTN CODE 54 DR RICHTER
SAN DIEGO CA 92152-5000

1

KWAJALEIN MISSILE RANGE
PO BOX 67
APO SAN FRANCISCO CA 96555

1

DEPARTMENT OF COMMERCE CTR
SUPPORT CTR LIBRARY R-51
TECHNICAL REPORTS
325 S BROADWAY
BOULDER CO 80303

1

DR HANS J LIEBE
NTIA ITS S 3
325 S BROADWAY
BOULDER CO 80303

1

NCAR LIBRARY SERIALS
NATIONAL CTR FOR ATMOS RESEARCH
PO BOX 3000
BOULDER CO 80307-3000

1

DEPARTMENT OF THE ARMY
ATTN DAMI POI
WASHINGTON DC 20310-1067

1

MIL ASST FOR ENV SCI OFC
OF THE UNDERSECRETARY OF DEFENSE
FOR RSCH & ENGR R&AT E&LS
PENTAGON ROOM 3D129
WASHINGTON DC 20301-3080

1

DEPARTMENT OF THE ARMY
DEAN RMD DR GOMEZ
WASHINGTON DC 20314

1

DIVISION OF ATMOSPHERIC SCIENCE
NATIONAL SCIENCE FOUNDATION
ATTN DR BIERLY
1800 G STREET NW
WASHINGTON DC 20550

1

SPACE & NAVAL WARFARE SYSTEM COMMAND
ATTN PMW 145 1G
WASHINGTON DC 20362-5100

1

NAVAL RESEARCH LABORATORY
ATTN CODE 4110 MR RUHNKE
WASHINGTON DC 20375-5000

1

ARMY INFANTRY
ATTN ATSH CD CS OR DR E DUTOIT
FT BENNING GA 30905-5090

1

USAFETAC DNE
SCOTT AFB IL 62225

1

AIR WEATHER SERVICE
TECHNICAL LIBRARY FL4414
SCOTT AFB IL 62225-5458

1

USAFETAC DNE
ATTN MR GLAUBER 1
SCOTT AFB IL 62225-5008

AWS DOO 1
SCOTT AFB IL 62225-5008

ARMY COMBINED ARMS COMBAT
ATTN ATZL CAW 1
FT LEAVENWORTH KS 66027-5300

ARMY SPACE INSTITUTE
ATTN ATZI SI 1
FT LEAVENWORTH KS 66027-5300

ARMY SPACE INSTITUTE
ATTN ATZL SI D 1
FT LEAVENWORTH KS 66027-7300

PHILLIPS LAB
ATTN PL LYP MR CHISHOLM 1
HANSCOM AFB MA 01731-5000

ATMOSPHERIC SCIENCES DIVISION
GEOPHYSICS DIRECTORATE
PHILLIPS LAB
ATTN DR MCCLATCHEY 1
HANSCOM AFB MA 01731-5000

RAYTHEON CO DR SONNENSCHN
EQUIPMENT DIVISION
528 BOSTON POST ROAD 1
SUDBURY MA 01776
MAIL STOP 1K9

ARMY MATERIEL SYSTEMS ANALYSIS ACTIVITY
ATTN AMXSY CR MR MARCHETTI 1
APG MD 21005-5071

ARMY MATERIEL SYSTEMS
ANALYSIS ACTIVITY
ATTN AMXSY MP MR COHEN 1
APG MD 21005-5071

ARMY MATERIEL SYSTEMS
ANALYSIS ACTIVITY
ATTN AMXSY AT MR CAMPBELL 1
APG MD 21005-5071

ARMY MATERIEL SYSTEMS
ANALYSIS ACTIVITY
ATTN AMXSY CS MR BRADLEY 1
APG MD 21005-5071

ARL CHEMICAL BIOLOGY
NUCLEAR EFFECTS DIVISION
ATTN AMSRL SL CO 1
APG MD 21010-5423

ARL
ATTN AMSRL D 1
2800 POWDER MILL ROAD
ADELPHI MD 20783-1145

ARL
ATTN AMSRL OP SD TP 1
TECHNICAL PUBLISHING
2800 POWDER MILL ROAD
ADELPHI MD 20783-1145

ARL
ATTN AMSRL OP CI SD TL 1
2800 POWDER MILL ROAD
ADELPHI MD 20783-1145

ARL
ATTN AMSRL SS SH 1
DR SZTANKAY
2800 POWDER MILL ROAD
ADELPHI MD 20783-1145

ARMY SPACE TECHNOLOGY
AND RESEARCH OFFICE
ATTN MS BRATHWAITE 1
5321 RIGGS ROAD
GAITHERSBURG MD 20882

NATIONAL SECURITY AGENCY
ATTN W21 DR LONGBOTHUM 1
9800 SAVAGE ROAD
FT G MEADE MD 20755-6000

OIC NAVSWC
TECHNICAL LIBRARY CODE E 232 1
SILVER SPRINGS MD 20903-5000

ARMY RESEARCH OFFICE
ATTN DRXRO GS DR FLOOD 1
PO BOX 12211
RTP NC 27009

DR JERRY DAVIS NCSU
DEPARTMENT OF MARINE EARTH AND
ATMOSPHERIC SCIENCES 1
PO BOX 8208
RALEIGH NC 27650-8208

ARMY CECRL ATTN CECRL RG DR BOYNE HANOVER NH 03755-1290	1
ARMY ARDEC ATTN SMCAR IMI I BLDG 59 DOVER NJ 07806-5000	1
ARMY SATELLITE COMM AGENCY ATTN DRCPM SC 3 FT MONMOUTH NJ 07703-5303	1
ARMY COMMUNICATIONS ELECTRONICS CTR FOR EW RSTA ATTN AMSEL EW MD FT MONMOUTH NJ 07703-5303	1
ARMY COMMUNICATIONS ELECTRONICS CTR FOR EW RSTA ATTN AMSEL EW D FT MONMOUTH NJ 07703-5303	1
ARMY COMMUNICATIONS ELECTRONICS CTR FOR EW RSTA ATTN AMSEL RD EW SP FT MONMOUTH NJ 07703-5206	1
DEPARTMENT OF THE AIR FORCE OL A 2D WEATHER SQUADRON MAC HOLLOMAN AFB NM 88330-5000	1
PL WE KIRTLAND AFB NM 87118-6008	1

ARMY TRADOC ANALYSIS CTR
ATTN ATRC WSS R
WSMR NM 88002-5502

1

ARMY WSMR
TECHNICAL LIBRARY BRANCH
ATTN STEWS IMIT
WSMR NM 88002

3

ARL BED
ATTN AMSRL BE MR VEAZY
WSMR NM 88002-5501

1

ARL BED
ATTN AMSRL BE A MR RUBIO
WSMR NM 88002-5501

1

ARL BED
ATTN AMSRL BE M DR NILES
WSMR NM 88002-5501

1

ARL BED
ATTN AMSRL BE W DR SEAGRAVES
WSMR NM 88002-5501

1

USAF ROME LABORATORY TECHNICAL
LIBRARY FL2810
CORRIDOR W STE 262 RL SUL
26 ELECTRONICS PARKWAY BLDG 106
GRIFFISS AFB NY 13441-4514

1

AFMC DOW
WRIGHT PATTERSON AFB OH 03340-5000

1

ARMY FIELD ARTILLERY SCHOOL ATTN ATSF TSM TA MR TAYLOR FT SILL OK 73503-5600	1
ARMY FIELD ARTILLERY SCHOOL ATTN ATSF F FD MR GULLION FT SILL OK 73503-5600	1
NAVAL AIR DEVELOPMENT CTR ATTN AL SALIK CODE 5012 WARMINSTER PA 18974	1
ARMY DUGWAY PROVING GROUND ATTN STEDP MT M M BOWERS DUGWAY UT 84022-5000	1
ARMY DUGWAY PROVING GROUND ATTN STEDP MT DA L DUGWAY UT 84022-5000	1
DEFENSE TECHNICAL INFORMATION CTR ATTN DTIC OCP CAMERON STATION ALEXANDRIA VA 22314-6145	2
ARMY OEC ATTN CSTE EFS PARK CTR IV 4501 FORD AVE ALEXANDRIA VA 22302-1458	1
ARMY FOREIGN SCIENCE & TECHNOLOGY CTR ATTN CM 220 7TH STREET NE CHARLOTTESVILLE VA 22901-5396	1

NAVAL SURFACE WEAPONS CTR	
CODE G63	1
DAHLGREN VA 22448-5000	

ARMY CORPS OF ENGINEERS	
ENGINEER TOPOGRAPHICS LABORATORY	
ATTN ETL GS LB	1
FT BELVOIR VA 22060	

ARMY TOPO ENGINEERING CTR	
ATTN CETEC ZC	1
FT BELVOIR VA 22060-5546	

USATRADO	
ATTN ATCD FA	1
FT MONROE VA 23651-5170	

TAC DOWP	1
LANGLEY AFB VA 23665-5524	

LOGISTICS CTR	
ATTN ATCL CE	1
FT LEE VA 23801-6000	

SCIENCE AND TECHNOLOGY	
101 RESEARCH DRIVE	1
HAMPTON VA 23666-1340	

ARMY NUCLEAR AND CHEMICAL AGENCY	
ATTN MONA ZB BLDG 2073	1
SPRINGFIELD VA 22150-3198	

Record Copy	18
-------------	----

Total	104
--------------	------------